Article

Not peer-reviewed version

TiO_2 and $CaCO_3$ Microparticles Produced in Aqueous Extracts from *Satureja montana*: Synthesis, Characterization and Preliminary Antimicrobial Test

Federica Valentini *, Irene Angela Colasanti, Camilla Zaratti, Dumitrita Filimon, Andrea Macchia, Anna Neri, Michela Relucenti, Massimo Reverberi, Ivo Allegrini, Ettore Guerriero, Marina Cerasa, Marta De Luca, Francesca Santangeli, Roberto Braglia, Francesco Scuderi, Lorenza Rugnini, Roberta Ranaldi, Roberto De Meis, Antonella Canini

Posted Date: 7 August 2025

doi: 10.20944/preprints202508.0473.v1

Keywords: *Satureja montana*; plant extract-functionalized microparticles; GC-MS extract analysis; oxygenated terpenoids as activator/phase controllers; Terpinene; Thymoquinone; Carvacrol; Thymol; L-Linalool; preliminary antimicrobial screening

 doi:10.20944/preprints202508.0473.v1

Article

TiO_2 and $CaCO_3$ Microparticles Produced in Aqueous Extracts from *Satureja montana:* Synthesis, Characterization and Preliminary Antimicrobial Test

Federica Valentini [1,*], Irene Angela Colasanti [1,2], Camilla Zaratti [1,2], Dumitrita Filimon [1], Andrea Macchia [3], Anna Neri [4], Michela Relucenti [5], Massimo Reverberi [6], Ivo Allegrini [7], Ettore Guerriero [8], Marina Cerasa [8], Marta De Luca [9], Francesca Santangeli [9], Roberto Braglia [10], Francesco Scuderi [10], Lorenza. Rugnini [10], Roberta Ranaldi [10], Roberto De Meis [10] and Antonella Canini [10]

[1] Sciences and Chemical Technologies Department, Tor Vergata University, Via della Ricerca Scientifica 1, 00133 Rome, Italy
[2] YOCOCU APS, Via Torquato Tasso 108, 00185 Rome, Italy
[3] Department of Biology, Ecology and Earth Sciences (DiBEST), University of Calabria, Via Pietro Bucci, 87036 Arcavacata, Italy
[4] Department of Biomedicine and Prevention, Tor Vergata University, Viale Montpellier 1, 00133 Rome, Italy
[5] Department of Anatomical, Histological, Forensic and Orthopaedic Sciences, Sapienza University of Rome, Via Alfonso Borelli 50, 00161 Rome, Italy
[6] Department of Environmental Biology, Sapienza University of Rome, Piazzale Aldo Moro 5, 00185 Rome, Italy
[7] Envint Srl, Via Paradiso 65a, 02034 Montopoli di Sabina, Rieti, Italy
[8] Institute of Atmospheric Pollution Research (IIA), National Research Council (CNR), Strada Provinciale 35d, 9, 00010 Montelibretti (RM), Italy
[9] Department of Physics, Sapienza University of Rome, Piazzale Aldo Moro 2, 00185 Rome, Italy
[10] Department of Biology, Tor Vergata University of Rome, Via della Ricerca Scientifica 1, 00133 Rome, Italy
* Correspondence: federicavalentini.chem@gmail.com

Abstract

The possibility of modifying the surface chemistry of materials, synthetizing inorganic particles in natural aqueous extracts of plants (at low temperature, avoiding calcination), opens the doors to undoubtedly very interesting scenarios for innovative functionalization strategies that are increasingly eco-sustainable and rich in interesting chemical-physical and biochemical properties. Among the aerial plant, *Satureja montana* exhibits interesting antibacterial, antifungal, antimicrobial and antioxidant activities due to the rich volatile and non-volatile compounds (as activators/phase controllers characterized by Gas Chromatography-Mass Spectrometry, GC-MS), contained in the aqueous extracts. For the first time, the aqueous extract of *Satureja montana* plant was applied for the green synthesis of TiO_2 and $CaCO_3$ particles, characterized by X-Ray diffraction (XRD), Raman, Infrared/IR spectroscopies, and Scanning Electron Microscopy-SEM/coupled by microanalysis EDX. Screening through antimicrobial assays under indoor passive sedimentation conditions showed opposite trends for both kind of inorganic particles. TiO_2 Anatase spherical particles ($400<\varphi<600$ nm) increase microbial growth, proportionally to increasing particles concentration (dose-dependent response). Probably, the low surface area (1.20 m^2/g), low porosity (pore volume 0.0023 cm^3/g; pore size of 560 nm) and smooth spherical morphology, don't provoke chemical or physical damages to microorganisms, and therefore microbial growth is not inhibited. This occurs in the presence of medium/low concentrations of ROS (oxygenated radical species), which are chemically active in generating oxidative stress and cell death. In fact, the chemically reactive defects found in these TiO_2/Anatase particles are predominantly carbonyl in nature, less reactive than carboxylic ones in producing ROS. Instead, S. montana-functionalized $CaCO_3$ prismatic microparticles (1µm x 1µm x

 doi:10.20944/preprints202508.0473.v1

1µm) exhibit strong and dose-dependent antimicrobial activities, achieving near-complete inhibition at 50 mg mL^{-1}. This could be related to the molecular activators/phase controllers that induced defects, edges, dislocations and chemical active surface functionalities on the prismatic calcite particles, making them capable of inhibiting microbial activity. In particular, the presence of carboxyl groups C=(O)-OH, recorded by FTIR on the prismatic surfaces of $CaCO_3$ MPs/SM particles, could be responsible for the production of ROS, the latter known to be dangerous sentinels of oxidative stress and cell death.

Keywords: *Satureja montana*; plant extract-functionalized microparticles; GC-MS extract analysis; oxygenated terpenoids as activator/phase controllers; Terpinene; Thymoquinone; Carvacrol; Thymol; L-Linalool; preliminary antimicrobial screening

1. Introduction

The possibility of synthesizing and especially functionalizing Micro and Nanomaterials in eco-sustainable work environments certainly opens the doors to new and interesting possibilities in obtaining smart nanomaterials with extraordinary chemical-physical [1], biochemical [2] and medical properties [3] of great relevance. For a long time, surface chemistry has been exclusively concerned with predominantly chemical functionalization reactions. The great variety of natural substances, such as essential oils [4]and natural extracts [5] from medicinal plants [6], allows to obtain (on a large scale mass production) increasingly eco-friendly micro; and nanomaterials characterized by excellent properties/features of clinical-medical [7], environmental [8], Cultural Heritage restoration/conservation [9]and food packaging interest [10]. Recently, several interesting review papers provide innovative advancements in green synthesis strategies to produce eco-friendly materials, focusing on raw materials, their reaction mechanism and surface Chemistry, challenges involved in different application fields [11–13].

The strategies based on the green synthetic approach offer several advantages over traditional mechanism production of new materials (as reported in **Scheme 1**). Traditional chemical synthesis routes are the subject of debate (in the international scientific community) because they involve the use of chemical reagents with an environmental impact and also contribute to the production of others (such as secondary waste products present in large volumes) that are difficult to dispose of in the environment [14]. Furthermore, conventional chemical synthesis involves much higher costs than strategies based on natural substances, easily available in the environment (at low cost and/or zero cost) and with low impact on humans, surfaces, materials and the ecosystem. The great advantage of using natural substances, present in the ecosystem, also allows the adoption of synthetic procedures that do not require high temperatures, high working pressures and non-aqueous solvents (which often produce reaction waste with a high impact on operators/end-users and the work environment). The ease of finding natural substances and their abundance allows for scaling up production to an industrial level, thus designing and creating new materials ready to be launched on the market [15]. In particular, several scientific publications dated 2025 (current year) focus on the scalable production of micro; and nanomaterials from extracts, essential oils and derivatives of natural plants [16–25]. The main reason is related to plants' widespread diffusion, to their medicinal and officinal properties, widely used in the past to heal, cure, nourish, purify (for example water) and to produce the colors used in classical Artworks (i.e., ancient Polychromy) [26].

The possibility of replicating processes that occur in Nature also represents a great scientific challenge because it would allow us to understand, simulate and reproduce completely spontaneous processes present in the World [27]. Not only that but simulating and reproducing many natural synthetic pathways would also guarantee the preservation of Nature and its vital processes, as well as the safeguarding of History (Our Past) through the care of Cultural Heritage (using the same raw materials, with which they were assembled in past eras of Human History) [28]. Among these new synthetic routes [16–25], those in which micro, and nanoparticles nucleate and subsequently grow,

 doi:10.20944/preprints202508.0473.v1

simultaneously with the extraction of natural substances from plants, are very interesting. In fact, natural substances that also play the role of "*templates in the green synthesis*" of particles have enormous advantages over chemical and/or physical templates, because they do not have to be removed at the end of the synthesis and become part of the surface functionalization [29–38]. Indeed, natural substances (contained in plant extracts, essential oils and exudates) usually known as biochemical additives, play the main role of phase controllers during green synthesis approach.

This new synthetic strategy is also fast on a time scale (no time consuming) because in a single reactive process the particles are produced from natural substances that shape them (in terms of shape, size and defects), also functionalizing them (in only "*one pot green synthetic approach*").

In this work, a simultaneous synthesis and functionalization process of TiO_2 and $CaCO_3$ microparticles (MPs), starting from natural extracts of *Satureja montana* (SM), was optimized. Especially, *Satureja montana* plant species (which is native from the Mediterranean region and cultivated all over Europe, Russia, and Turkey [39,40]) has been selected because of interesting antimicrobial properties, the great potential synergism with antibiotics, anti-inflammatory, antibacterial, antifungal, and antioxidant features [41–45]. Recently, Rai et al. (2025) [46] demonstrate the high efficiency of the synergistic combinations with two well-known antibiotics (gentamicin and amphotericin B) and Essential Oils (EOs), this latter extracted from SM, against a panel of pathogenic bacteria and candida (responsible for the extensive formation of biofilms on polymaterial surfaces). Natural Plant Extracts (NPEs), EOs and phytochemicals represent a smart alternative strategy to control Salmonella biofilm formation [47]. Thymol, carvacrol, and eugenol, notably from different SM species, exhibit excellent antibiofilm activity, inducing stress-related proteins in Salmonella. Plant-derived extracts and phytochemicals (including plant extracts, essential oils, and purified phytochemicals, individually or combined ones) act against both planktonic and biofilm forms by disrupting biofilm formation, motility and surfaces adhesion. Phyto-synthesized microparticles offer a very promising approach, combating microbial biofilms while being cost-effective, environmentally friendly and highly compatible with the polymaterial surfaces to be treated and with the end-users [47]. Integrating plant extracts and synthetic microparticles demonstrates potential in addressing biofilm-related issues and antibiotic resistance (fundamental features for applications in the medical, pharmacological, nutritional fields and also for the conservation of Cultural Heritage). For this purpose, during the past time, Rinaldi et al. (2021) [48] optimized Nano-Emulsion (NEs) formulations to ensure food safety quality and counteract the antibiotic resistance of poultry associated *E. coli*, if applied in poultry farms. To improve the essential oils (EO) properties, oil in water Nano-Emulsions (NEs) composed of SMEOs (*Satureja montana* Essential Oils) and Tween-80 were synthetized, fully characterized, and their antimicrobial and antibiofilm properties assayed against *Escherichia coli* strains isolated from healthy chicken. Since surfactant and oil composition can strongly influence NE features and their application fields, a ternary phase diagram was evaluated to select the best surfactant/oil/water ratio composition.

During 2021, Oliveira-Pinto et al. [49] combined SMEOS with the Zein microparticles (ZNPs) in an optimized formulation suitable to reduce the *X. euvesicatoria* (Xeu) amount, which is responsible for the Tomato Bacterial spot (Bs), and simultaneously to improve plants' health, mainly for their antimicrobial activity on Xeu pathogens. In the following year 2022, the same authors Oliveira-Pinto et al. [50] report about the Nano clays production and characterization, such as Montmorillonite (NMT), demonstrating their excellent antimicrobial activities, or their role as delivery tools/stabilizers for organic compounds, such as natural extracts from plants and/or essential oils (EOs), which also exhibit antimicrobial activity against plant pathogens [50]. Results highlight that the NMT was able to reduce Xeu bacterial amount, while reducing ROS (Radical Oxygenated Species) production and keeping the transcript levels of the defense-related genes close to those of the control samples (used for comparison). Generally, the results show that NMT has a great potential to integrate Bs management approaches, considering its antimicrobial activity, and that EO and/or Nano clays could be successfully employed as new disease preventive strategies, since they enhance the healthy shoots' defense, thus potentially reducing the pathogen establishment.

 doi:10.20944/preprints202508.0473.v1

Currently, SM has never been used to synthesize/functionalize with its extracts, TiO_2 and $CaCO_3$ microparticles (MPs) as done in this work, which for this reason is innovative (in terms of products synthesized and characterized). According to this, TiO_2 nanoparticles (i.e., TiO_2 NPs) have been previously synthetized and functionalized by applying *Jasminum* and *Magnolia champaca* flower extracts, as reported by Sangeetha et al. (2024) [51]. These authors demonstrate that NPs synthesis applying natural extracts/oils led to rutile phase of TiO_2 NPs while chemical synthesis produced anatase phase. Green synthesis yielded larger crystallite size TiO_2 compared to chemical synthesis, also enhancing the photoluminescence emission efficiency. In this current year 2025, Pham et al. [52], for the first time, fabricate innovative aqueous Nano Emulsions (NEs) based on anthraquinone-rich extract of *P. cuspitaum* and TiO_2 nanoparticles, together with surfactants, evaluating the corresponding antifungal efficiencies, against the melon fungal diseases. At a concentration of 0.5%, the NE formulation completely inhibited the mycelial growth of *Botrytis cinerea*, *Phytophthora spp*., *Fusarium oxysporum*, *Colletotrichum spp*., *Sclerotium spp*., *Rhizoctonia spp*., and the germination of *Eryshipe cichorasearum spores*, respectively [52]. Other authors, as Wang et al. (2025) [53], develop a new chitosan-based nanocomposite films incorporating nano-TiO_2 and Daisy Essential Oil for the preservation of *Actinidia arguta* (which represents a small fruit rich in many vitamins and minerals especially vitamin C is much higher than other fruits [54]. The films exhibited enhanced mechanical strength, antimicrobial activity, and antioxidant capacity. Application of these nanocomposite films on *Actinidia arguta* reveals significant improvements in weight loss, hardness, decay rate, total microbial count, respiration rate, soluble solids content, vitamin C, titratable acidity, and enzyme activities during food storage. Experimental data show that chitosan/nano-TiO_2/DEO nanocomposite films effectively extend the shelf life and preserve the quality of *Actinidia arguta*, providing a promising strategy for the natural and eco-sustainable food preservation chain.

According to these literatures, TiO_2 particles described above have been synthetized by calcination treatments, carried out at high temperatures [55], instead, we propose a sustainable low-temperature method (avoiding calcination), as already reported by Prof. Eckhart Wollenweber [56]. This latter, which allows to produce particles in the aqueous natural extracts of SM at lower temperatures, result useful to study exudate/extract flavonoids but without removing Volatile Organic Compounds (VOCs), which are responsible for the main antibacterial, antimicrobial, antifungal, antioxidant and photocatalytic properties, opening up a range of application opportunities in many industrial sectors.

Even more innovative is the approach performed in this work, regarding the synthesis and functionalization of calcite microparticles ($CaCO_3$ MPs) with SM extract (for the first time synthetized here). Indeed, starting from 2023 some authors such as Meydan et al. (2023) [57], describe the green synthesis of calcium carbonate nanoparticles ($CaCO_3$ NPs), by applying the Gum Arabic, as a natural polymer for green synthesis. The synthesized $CaCO_3$ NPs showed good photocatalytic activity to methylene blue (MB) dye degradation, which percentage degradation was 93% after 120 min. Also, the cytotoxicity of $CaCO_3$ NPs has been examined on the normal L929 and cancer CT26 cell lines and the IC_{50} value was about 250 μg/mL for cancer cells [57]. During the same year, other authors as Nelwamondo et al. (2023) [58], demonstrate the MgO and $CaCO_3$/Moringa oleifera nanoparticles production and assessed the green nanoparticles effects on groundnut genotypes. The effect of biosynthesized MgO and $CaCO_3$ nanoparticles (NPs) using *Moringa oleifera* natural extract on the growth and yield of groundnut genotypes (exposed to different concentrations of green NPs) has been widely investigated [58]. The findings demonstrated that foliar application of MgO/$CaCO_3$/*Moringa oleifera* natural extract NPs positively affected groundnut biomass production. There is a great deal of evidence signifying that foliar applications of 50 mg/L of MgO 100 mg/L $CaCO_3$ contributed greatly to plant growth and crop production, and for this purpose the green NPS are very recommended as Nano-fertilizers application rate for groundnut production [58].

In our very recent publications cited as Valentini et al. (2024) [59], authors report about the use of Fe-Alg-$CaCO_3$ microparticles (MPs) as foliar fertilizer on lettuce plants in an aquaponic system. MPs were produced starting from $CaCO_3$ nanoparticles (used here as precursors of MPs), these latter

 doi:10.20944/preprints202508.0473.v1

synthetized by applying a biomimetic approach, optimized by Valentini et al. (2022) [60]. The research investigated *Lactuca sativa L. cv. Foglia di Quercia Verde* plants as the experimental cultivar. Three iron concentrations (10, 50, and 250 ppm) were tested, with 15 plants per treatment group, plus a control group receiving only sterile double-distilled water. This study investigated rosette diameter, root length, fresh weight, soluble solids concentration, levels of photosynthetic pigments, and phenolic and flavonoid content. The optimized concentration of 250 ppm for treatment provided the most significant enhancements in both biomass yield and quality, highlighting the potential of precision fertilizers to boost eco-sustainability and efficiency in aquaponic systems. During 2025, Valentini et al. [61], add a further important scientific result concerning the application of green Zn-Alg-$CaCO_3$ MPs as an eco-sustainable solution for precision fertilization of Tomato plants (*Solanum lycopersicum L. cv. Principe Borghese*) in aquaponic agriculture approach. Several parameters have been investigated as antioxidant activity, phenolic, flavonoid, and lycopene contents, which particularly enhanced at the highest concentrations of green Zn-Alg-$CaCO_3$ MPs. Importantly, no increase in zinc element was detected in recirculating water, highlighting the environmental safety of foliar application. These experimental results highlight the potential of Zn-Alg-$CaCO_3$ MPs as a sustainable solution for precision fertilization in aquaponic agriculture. According to this, the authors wanted to combine for the first time the exceptional properties of natural SM extracts (especially the anti-biofilm features) with the production and functionalization of microstructured calcite ($CaCO_3$ MPs), to be used in fields other than those widely reported in this introduction, such as the conservation and restoration of Cultural Heritage and Historical-Artistic Heritage/surfaces. During the past time, in our previous work [62], we demonstrated that homemade $CaCO_3$ nanoparticles/nanofiller were successfully employed for reinforcing the plaster of Palazzetto Alessandro Lancia in Rome (Italy). During 2017, Valentini et al. [63] described the role of nanostructured $CaCO_3$ for the deacidification of Library and Archival Materials (i.e., indoor Cultural Heritage). Furthermore, Valentini et al. (2022) [60] applied $CaCO_3$ nanoparticles for the consolidation of Pietraforte (a particular type of Florentine sandstone) which makes up the Bell Tower of San Lorenzo (belonging to the corresponding monumental complex of San Lorenzo), in Florence (Italy).

Considering all this, the aim of this work is to synthesize inorganic particles (i.e., TiO_2 and $CaCO_3$) having a green and sustainable chemistry approach (based on SM's aqueous extract, carried out at low temperatures), which encompasses many interesting antimicrobial features for future applications in many fields, such as clinical-medical, pharmaceutical, nutraceutical, food chemistry, agricultural and even in the conservation of Cultural Heritage.

Finally, for clarity of discussion in the text, **Scheme 2** reports the nomenclature of the materials cited and applied in the work, including the acronyms and abbreviations used.

 doi:10.20944/preprints202508.0473.v1

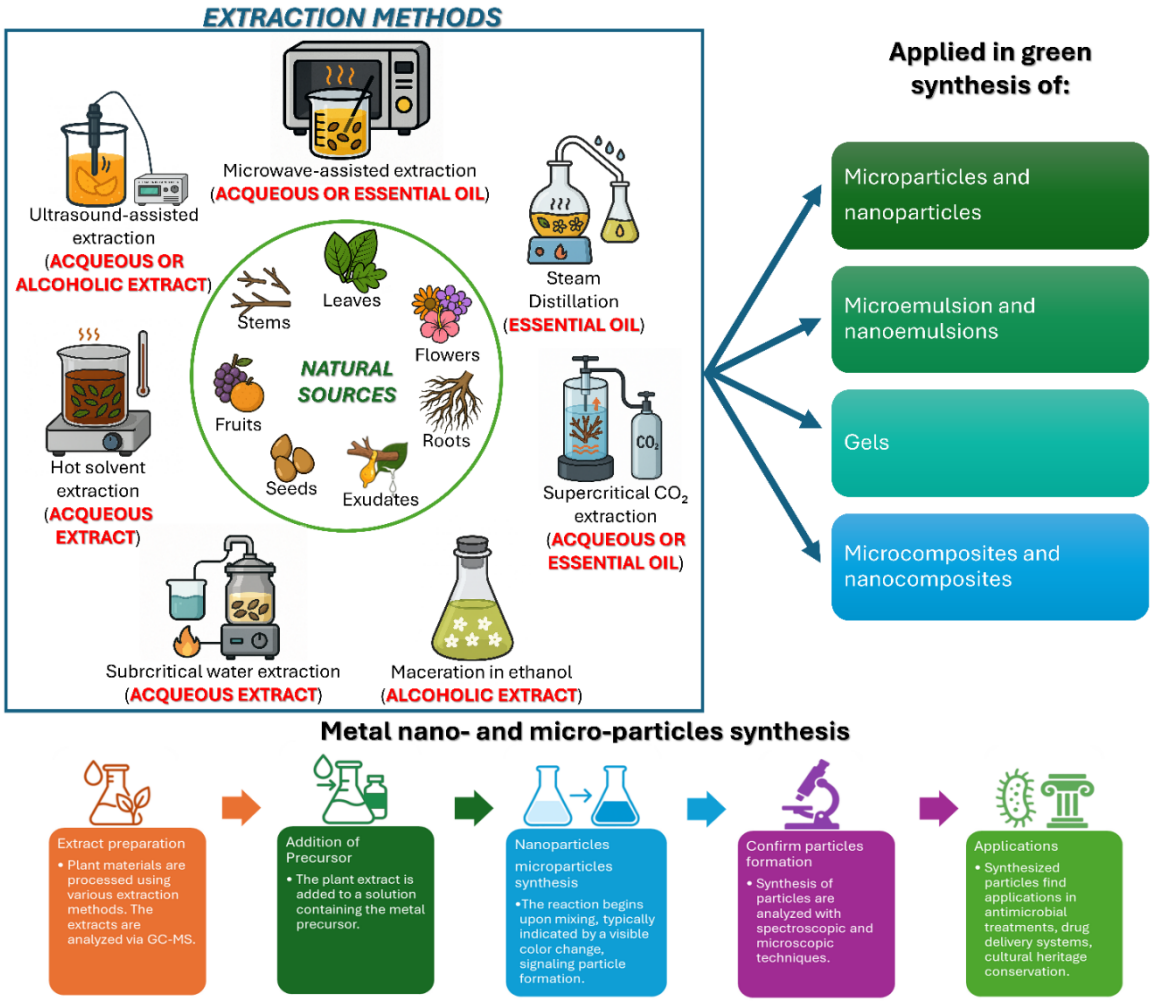

Scheme 1. Green synthesis routes for the functionalization of micro- and nanoparticles using natural extracts, essential oils and exudates from natural plants.

Scheme 2. Nomenclature, acronyms/abbreviations, description of all materials cited in the text.

Nomenclature	Acronyms abbreviations	Description	Notes
Titanium Oxide	TiO_2 MPs/SM	Functionalized particles produced in natural extracts of plants	Microparticles (in size) as confirmed in this work
Calcium Carbonate	$CaCO_3$ MPs/SM	Functionalized particles produced in natural extracts of plants	Microparticles (in size) as confirmed in this work
Microparticles	MPs	Microparticles are tiny spherical particles, typically ranging from 1 to 1000 micrometers in diameter.	Microparticles used for biological assay in this work
Nanoparticles	NPs	Nanoparticles are incredibly small particles, typically between 1 and 100 nanometers in size	[1]
Satureja montana	SM	Plant species, which is native from the Mediterranean region and cultivated all over Europe, Russia, and Turkey	*Satureja montana L., Lamiaceae*, commonly known as winter savory This work
Natural Plant Extracts	NPEs	Extracts may be derived from whole plants or from specific parts of plants	Natural Extracts (by drying the leaves of the

 doi:10.20944/preprints202508.0473.v1

		such as leaves, stems, barks, roots, flowers and/or fruits	plants) were performed at low temperature and in bi-distilled water. This work
Essential Oils	EOs	Essential Oils are precious mixtures of liquid and volatile aromatic substances, extracted mainly by steam distillation from plant material coming from various types of aromatic plants; they can also be obtained by cold pressing, as in the case of oils derived from citrus peel or by solvent extraction.	[47–50]
Nano-Emulsions	(NEs)	Nanoemulsions are nano-sized emulsions (20–200 nm), thermodynamically stable isotropic system in which two immiscible liquids are mixed to form a single phase	[48–50]
Satureja montana Essential Oils and Tween-80	SMEOs	Oil in water Nano-Emulsions (NEs) composed of SMEOs (*Satureja montana* Essential Oils) and Tween-80	[48,49]
Montmorillonite	NMT	Montmorillonite is a naturally occurring clay mineral belonging to the smectite group, primarily of aluminosilicate	[50]
Chitosan-nano-TiO_2 Daisy Essential Oil	chitosan/nano TiO_2/DEO	Chitosan film, incorporating nano-TiO_2, functionalized with Daisy Essential Oil	[53,54]
Magnesium Oxide and Calcium Carbonate *Moringa oleifera* natural extract	MgO/$CaCO_3$/ Moringa oleifera NPs	Biosynthesized MgO and $CaCO_3$ nanoparticles (NPs) using *Moringa oleifera* natural extract	[58]
Iron-Calcium Alginate-Calcium Carbonate microparticles/microspheres	Fe-Alg-$CaCO_3$ MPs	Foliar fertilizer on lettuce plants in an aquaponic system	[59]
Zinc- Alginate-Calcium Carbonate microparticles	Zn-Alg-$CaCO_3$ MPs	eco-sustainable solution for precision fertilization of Tomato plants in aquaponic agriculture approach	[61]
Volatile Organic Compounds	VOCs	Volatile organic compounds are a group of chemicals that easily evaporate at room temperature and are commonly found in various products used indoors and outdoors (in this study terpenes family)	[56]
Methylene Blue	MB	Methylene blue is used as a bacteriologic stain or dye and indicator	[57]
Radical Oxygenated Species	ROS	Reactive Oxygen Species (ROS) are unstable, highly reactive molecules containing oxygen that can cause damage to cells by reacting with other molecules.	[49,50,64,65]

2. Results and Discussion

 doi:10.20944/preprints202508.0473.v1

This chapter is organized as follows: first, the results related to the morphological and structural characterization of the new functionalized microparticles are reported and described. Then, the chemical composition of the natural SM extracts is discussed, by means of GC-MS analysis; and finally, the results related to the study of the antibacterial, antimicrobial, antioxidant and antibiofilm properties, found in appropriate bacterial strains selected and treated at different concentrations of new functionalized particles, are widely reported and discussed.

2.1. Functionalized Microparticles and Their Characterization Study

2.1.1. TiO_2 MPs/SM

The TiO_2 particles contained in the alcoholic suspension, shows instead a spherical shape, with diameters ranging from 160 nm to 1.3 µm, with a prevalence of elements with diameters around 400-600 nm (**Figure 1 A**). The surface of the micro/nanospheres appears smooth and the observations at high magnification (**Figure 1 B**) suggest that the spherical elements have variable sizes because they arise from the nucleation of TIO_2 around a core of amorphous organic substance and then they gradually growth in size by TIO_2 apposition. The amorphous aggregates of organic matter are indicated by the arrows in **Figure 1 B**.

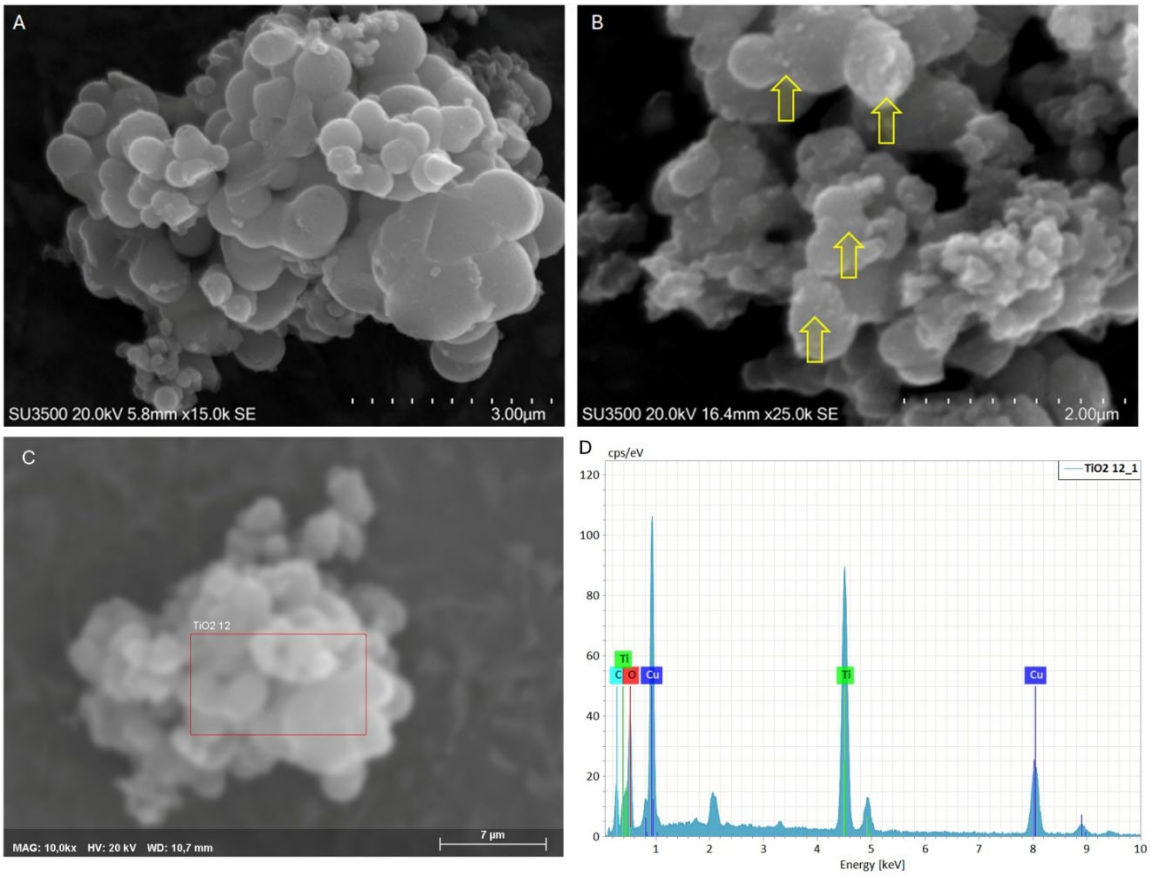

Figure 1. SEM of TiO_2 microspheres. **A**) a microspheres cluster is presented, spherical structures are visible, with variable sizes ranging from 160nm up to 1.3 µm, magnification 10K. **B**) A higher magnification of a microspheres cluster shows the amorphous organic material on the surface of microparticles (arrows), magnification 25 K. **C**) and **D**) highlight the microanalysis, where: **C**) is the SEM image of the examined sample, the red rectangle shows the ROI from which the spectrum was extracted; **D**) is the spectrum clearly shows the titanium/Ti peak; the copper peaks are due to the grid on which the sample was deposited. The other elements are C and O.

The XRD analysis revealed a slightly noisy diffractogram (**Figure 2A**) characterized by broad peaks centered at 11.74°, 17.45°, 21.77°, 24.60°, 27.91°, 30.54°, 32.90°, and 35.63° (2θ, Mo Kα). All

 doi:10.20944/preprints202508.0473.v1

detected reflections were attributed to the anatase phase of TiO_2, with the most intense peak at 11.74°, corresponding to the (101) plane [66–68]. The remaining signals were assigned to the (112), (200), (211), (204), (220), (301), and (312) planes, respectively. Nevertheless, the presence of brookite (~10%) cannot be entirely ruled out, as the peaks at 11.74° and 21.77° may also match the (111) and (231) planes of this TiO_2 polymorph [68,69]. However, the absence of the typical high-intensity doublet that characterizes the brookite phase suggests that the sample is predominantly composed of the anatase form (~90%).

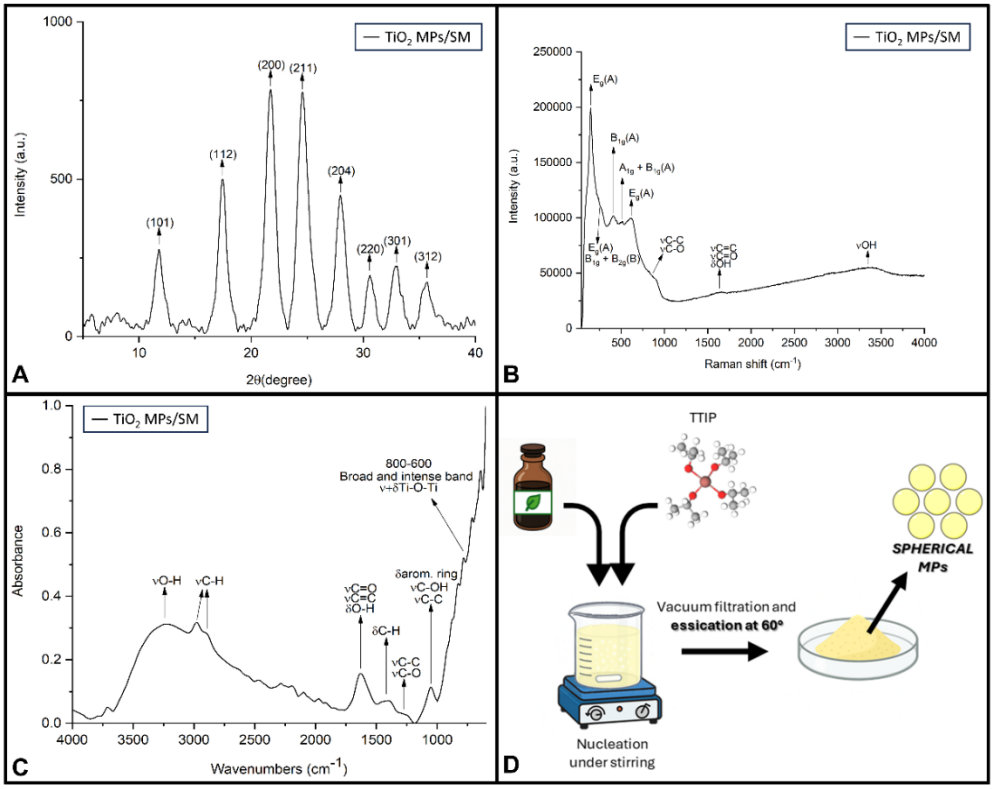

Figure 2. XRD (**A**); Raman (**B**) and FTIR (**C**) for TiO_2 MPs/SM. (**D**): scheme of spherical TiO_2 synthesis.

Raman spectroscopy provided further confirmation of the TiO_2 crystalline phases (**Figure 2B** and **Table 1**). The spectrum revealed the presence of characteristic bands of the anatase polymorph, confirming the results obtained by XRD analysis. A strong band was observed at 146 cm^{-1}, corresponding to the E_g vibrational mode of anatase, along with the B_{1g} mode at 411 cm^{-1}. Additional bands were detected at 517 cm^{-1} and 623 cm^{-1}, attributable to the $A_{1g} + B_{1g}$ and E_g modes of the anatase phase, respectively [70–72]. Two minor shoulders were also observed between 219 cm^{-1} and 279 cm^{-1}, which can be attributed to the B_{1g} and B_{2g} vibrational modes of brookite, suggesting the possible presence of this secondary polymorph in low concentration [72,73]. Nevertheless, a partial contribution from the low-frequency E_g mode of anatase, typically appearing as a broad shoulder around 200 cm^{-1}, cannot be excluded [70–72]. In addition, the Raman spectrum exhibited broad fluorescence related features at ~ 874, ~ 1627, and ~ 3352 cm^{-1}, which are likely associated with the vibrational modes of the organic functional groups/phase controllers used to functionalize/draw the particles (see **Figure S3** in Supplementary Information). Specifically, the band at 874 cm^{-1} may correspond to ν(C–C), ν(C–O) stretching and δ(C–H) bending vibrations, while the band at 1627 cm^{-1} may arise from ν(C=C) or ν(C=O) stretching, as well as δ(O–H) bending [74–83]. The broad signal at 3352 cm^{-1} is attributable to ν(O–H) stretching vibrations, indicative of hydroxyl groups of phytocompounds based activators [84].

FTIR-ATR analysis confirmed the successful synthesis and functionalization of TiO_2 nanoparticles with *Satureja montana* extract (**Figure 2C**). A broad and intense absorption band

 doi:10.20944/preprints202508.0473.v1

observed in the range 800–600 cm^{-1} was attributed to Ti–O–Ti stretching and bending vibrations, typical of titanium dioxide frameworks [85,86]. Signals at approximately 3400 cm^{-1} and 1630 cm^{-1} were assigned to O–H stretching and bending vibrations, respectively, indicating the presence of hydroxyl groups, either due to surface hydroxylation or originating from phenolic and terpenoid constituents of the plant extract [87–91]. Additionally, the spectrum displayed several distinctive bands associated with phytocompounds from the extract. Notably, peaks at 2974 cm^{-1} and 2893 cm^{-1} correspond to the asymmetric stretching of $–CH_3$ groups and the symmetric stretching of $–CH_2$ groups, respectively. Absorption bands between 1454 and 1395 cm^{-1} were assigned to C–H bending vibrations, specifically the asymmetric and symmetric bending modes of methyl and methylene groups. Furthermore, the band at 1268 cm^{-1} was attributed to C–O stretching vibrations, while the signal at 1051 cm^{-1} indicated C–O or C–C stretching modes [90,91]. All the FTIR band assignments are also reported in **Table 1**.

Table 1. Raman and FTIR band assignments of TiO_2 MPs /SM.

Band (cm^{-1})	Assignment	Ref.
RAMAN SPECTROSCOPY		
146	E_g mode (anatase)	[70–72]
219-279	E_g (anatase) $B_{1g} + B_{2g}$ mode (brookite)	[70–73]
411	B_{1g} mode (anatase)	[70–72]
517	$A_{1g} + B_{1g}$ mode (anatase)	[70–72]
623	E_g mode (anatase)	[70–72]
~874	νC–OH νC–C δCH/CH_2	[74–83]
~1627	νC=O νC=C δO-H	[74–82]
~3352	νO-H	[84]
FTIR SPECTROSCOPY		
3400	νO–H	[87–91]
1630	δO–H νC=O νC=C	[87–91]
2974	ν_{as} $–CH_3$	[90,91]
2893	ν_s $–CH_2$	[90,91]
1454, 1395	$\delta_{as/s}$ $–CH_3$ $\delta_{as/s}$ $–CH_2$	[90,91]
1268	νC–O νC–C	[90,91]
1051	νC–O νC–C ring vibration	[90,91]
800-600	ν+δ Ti–O–Ti	[85,86]

Vibrational bands assignments follow conventional spectroscopic notation: ν = stretching; δ = bending; s = symmetric; as = asymmetric.

2.1.2. $CaCO_3$ MPs/SM

The $CaCO_3$ particles in the examined alcohol suspension, appear as crystals with a prismatic shape, sharp edges and variable size (Figure 3 A), with an average of 1 μm x 1 μm x 1 μm. Amorphous aggregates of organic matter (indicated by the arrows in **Figure 3 B**) are adherent onto the smooth

 doi:10.20944/preprints202508.0473.v1

surface of the crystals. The image B (high magnification) shows that the prismatic crystals' structure is the result of a stratification of thin and smooth plates (like cheddar cheese layered tiles).

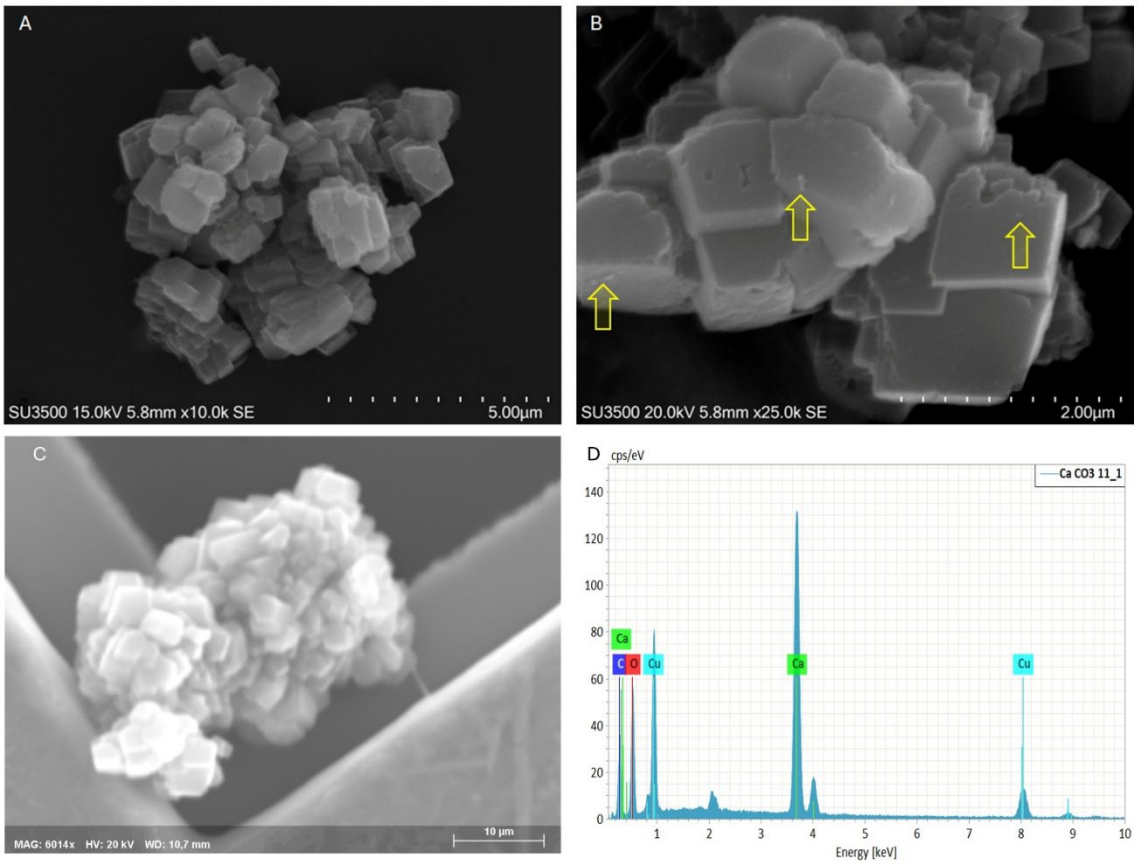

Figure 3. SEM of $CaCO_3$ Crystal. **A**) a crystal cluster is presented, prismatic structures with sharp edges are visible, one on the top of each other, magnification 10K. **B**) A higher magnification of a Crystal cluster shows the amorphous organic material on the surface of prismatic crystals (arrows), and evidence that they are formed by a layered structure of thin plates, magnification 25 K. **C**) and **D**) highlight the microanalysis, where: **C**) is SEM image of the examined sample, the red rectangle shows the ROI from which the spectrum was extracted; **D**) is the spectrum clearly shows the calcium/Ca peak; the copper peaks are due to the grid on which the sample was deposited. The other elements are C and O.

The diffractogram obtained for $CaCO_3$ MPs/SM reveals calcite as the predominant crystalline phase (**Figure 4A**). The most intense diffraction peak is observed at $2\theta = 29.43°$, corresponding to the (104) plane, a characteristic reflection of calcite [92–95]. Additional peaks, including those at 31.46°, 56.54°, and beyond 58.20°, exhibit lower intensities. Nevertheless, the overall diffraction pattern unambiguously confirms the presence of calcite, with no significant traces of other $CaCO_3$ polymorphs [92–95]. These findings suggest that *Satureja montana* extract favors the formation of the calcitic phase over other crystalline structures (i.e., predominant phase).

 doi:10.20944/preprints202508.0473.v1

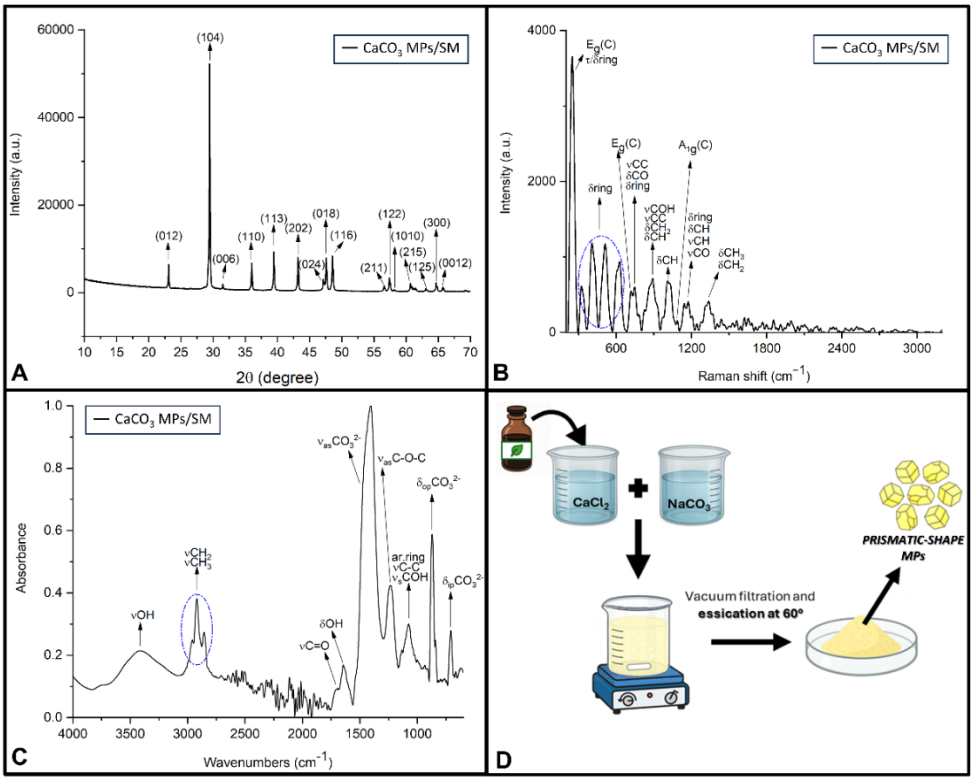

Figure 4. XRD (**A**); Raman (**B**) and FTIR (**C**) of $CaCO_3$ MPs/SM. (**D**): scheme of polygonal $CaCO_3$ synthesis.

Complementary insights were provided by Raman spectroscopy, which revealed vibrational features attributable to both the calcitic phase and organic phytocompounds introduced by SM extract during synthesis (**Figure 4B,** and **Table 2**). The presence of calcite is confirmed by the bands at 248 cm^{-1}, 718 cm^{-1}, and 1092 cm^{-1}. Specifically, the 1092 cm^{-1} band corresponds to the symmetric stretching vibration of the CO_3^{2-} group (A_{1g} mode), while the 718 cm^{-1} band is attributed to the in-plane bending vibration of the carbonate ion (E_g mode) [96,97]. The signal at 248 cm^{-1} relates to lattice translational vibrations (E_g mode) but may also partially overlap with skeletal torsional and deformation modes of aromatic phytocompounds, suggesting nanoparticle surface functionalization [74–78,82]. Moreover, other spectral bands support the presence of flavonoids and phenolic terpenoids on the carbonate surface. In the low-frequency region, several additional Raman bands (320, 412, 507, and 626 cm^{-1}) are assigned to skeletal deformations, twisting, and out-of-plane vibrations of aromatic ring systems [74–78,82].

The band at 746 cm^{-1} arises from a combination of C–C stretching, C–O bending, and aromatic ring deformation, while the signal at 890 cm^{-1} is linked to C–OH and C–C stretching, as well as CH and CH_2 bending vibrations [74–78,82]. Other bands such as 1009 cm^{-1} and 1180 cm^{-1} are attributed to in-plane CH bending, C–O stretching, and aromatic skeletal vibrations, whereas the band at 1339 cm^{-1} is associated with CH_3 bending (notably of isopropyl groups) and CH_2 scissoring modes [74–82].

The FTIR spectrum further confirms the dual nature of the material, revealing contributions from both the inorganic carbonate phase and the organic constituents (**Figure 4C**, and **Table 2**). The bands at 1404 cm^{-1} and 870 cm^{-1} correspond to the asymmetric stretching and out-of-plane bending vibrations of CO_3^{2-}, respectively. The additional signal at 705 cm^{-1}, attributed to in-plane bending of CO_3^{2-}, confirms the identification of the calcite phase [98,99]. A broad band in the 3600–3000 cm^{-1} range is assigned to O–H stretching vibrations, originating from adsorbed water, surface hydroxyl groups, and phenolic or alcoholic phytocompounds. The presence of aliphatic chains, typical of plant-derived molecules, is confirmed by the bands at 2951, 2922, and 2856 cm^{-1}, which are associated with asymmetric and symmetric C–H stretching vibrations of methyl (CH_3) and methylene (CH_2) groups

 doi:10.20944/preprints202508.0473.v1

[87–91]. A sharp absorption band at 1710 cm^{-1} corresponds to carbonyl (C=O) stretching, while the band at 1637 cm^{-1} is mainly due to molecular water bending (δO–H), with potential contributions from C=O and C=C stretching vibrations in aromatic systems [87–91]. Finally, the bands at 1231 cm^{-1} and 1070 cm^{-1} are assigned to C–O and C–C stretching modes, as well as to skeletal vibrations of aromatic rings, further confirming the presence of oxygenated phytocompounds on the nanoparticle surface.

Table 2. Raman and FTIR band assignments of $CaCO_3$ MPs /SM.

Band (cm^{-1})	Assignment	Reference
RAMAN SPECTROSCOPY		
248	E_g lattice mode (calcite) τ+δ aromatic ring	[96,97]
320	τ aromatic ring	[74–78,82]
412	δ_{op}+τ aromatic ring	[74–78,82]
507	δ_{op} +τ aromatic ring	[74–78,82]
626	δ_{op} +τ aromatic ring	[74–78,82]
718	E_g mode ($\delta_{ip}CO_3^{2-}$) (calcite)	[96,97]
746	νC–C δC–O δ aromatic ring	[74–78,82]
890	νC–OH νC–C δCH/CH_2	[74–78,82]
1009	δ_{ip}CH νC–O δ aromatic skeletal	[75–82]
1092	A_{1g} mode ($\nu_sCO_3^{2-}$) (calcite)	[96,97]
1180	δCH νC–O δ aromatic skeletal	[74–83]
1339	δCH_3 (isopropyl) δCH_2	[74–83]
FTIR-ATR SPECTROSCOPY		
3600-3000	νO–H	[88–91]
2951	ν_{as} –CH_3	[87–91]
2922	ν_{as} –CH_2	[87–91]
2856	ν_s –CH_2	[87–91]
1710	νC=O	[87–91]
1637	δO–H νC=O νC=C	[87–91]
1404	$\nu_{as}CO_3^{2-}$ (calcite)	[98,99]
1231	νC–O νC–C δ aromatic skeletal	[87–91]
1070	νC–O νC–C δ aromatic skeletal	[87–91]
870	$\delta_{op}CO_3^{2-}$ (calcite)	[98,99]

 doi:10.20944/preprints202508.0473.v1

705	$\delta_{ip}CO_3^{2-}$ (calcite)	[98,99]

Vibrational bands assignments follow conventional spectroscopic notation: ν = stretching; δ = bending; τ = twisting; s = symmetric; as = asymmetric; ip = in-plane; op = out-of-plane.

2.2. Chemical Composition of NPEs from SM by GC-MS

GC-MS analyses were performed using both targeted and untargeted approaches to comprehensively characterize the volatile fraction of the *Satureja montana* aqueous extract (SM). The integration of both methods allowed not only the identification of a defined set of known volatile constituents but also the detection of additional, previously unconsidered compounds, potentially involved in the green synthesis and surface functionalization of microparticles.

2.2.1. Targeted Analysis

A targeted GC-MS analysis was performed on the aqueous extract of SM immediately after preparation, with the aim of characterizing its volatile composition and identifying compounds potentially involved in the surface functionalization of microparticles. The analysis was carried out using a calibrated terpene standard mixture, allowing the semi-quantitative determination of 24 selected volatile organic compounds (see **Table 3**).

Table 3. Semi-quantitative concentrations of VOCs identified by targeted GC-MS (n.d. = not detected).

Compound	Concentration [ng/ml]
α-Thujone	282
α-pinene	n.d.
Camphene	n.d.
Sabinene	1054
β-Pinene	n.d.
α-Phellandrene	264
α-Terpinene	3814
para-cymene	157
(R)-(+)-Limonene	535
α-Terpinolene	284
γ-Terpinene	882
Terpinen 4-ol	10305
Carvacrol methyl ether	23.4
L-Carvone	n.d.
Thymoquinone	8271.
Geraniol	n.d.
Thymol	63906
Carvacrol	5669
β-Caryophyllene	n.d.
α-Humulene	4.0
caryophyllene oxide	135
cis-α-bisabolene (Levomenol)	4.7
L-Linalool	1425
aromadendrene oxide 2	n.d.

The extract was dominated by oxygenated monoterpenes, with thymol being by far the most abundant constituent (63,906 ng/mL), followed by terpinen-4-ol (10,305 ng/mL) and thymoquinone (8,271 ng/mL). Other noteworthy compounds included γ-terpinene (882 ng/mL), carvacrol (5,669 ng/mL), α-terpinene (3,814 ng/mL), and sabinene (1,054 ng/mL). The presence of α-thujone (282

 doi:10.20944/preprints202508.0473.v1

ng/mL), α-phellandrene (264 ng/mL), and α-terpinolene (284 ng/mL) further confirmed the richness of the terpene fraction. Trace amounts of carvacrol methyl ether (23 ng/mL), caryophyllene oxide (135 ng/mL), L-linalool (1,425 ng/mL), and para-cymene (157 ng/mL) were also identified.

The volatile profile of the extract included monoterpene hydrocarbons (e.g., sabinene, α-thujone, α-terpinene), oxygenated derivatives (e.g., thymol, terpinen-4-ol, caryophyllene oxide), and aromatic compounds (e.g., p-cymene, thymoquinone), reflecting a chemically diverse composition.

Notably, thymol and terpinen-4-ol showed the highest peak areas, followed by thymoquinone, carvacrol, and α-terpinene, while compounds like caryophyllene oxide and l-linalool were present at lower levels. This distribution confirms the predominance of oxygenated monoterpenes among the most abundant constituents.

The analysis was conducted on a single, well-characterized extract, providing a representative chemical fingerprint under the tested conditions. Although the lack of replicates prevents statistical evaluation, the dataset offers a consistent reference for subsequent applications using the same preparation.

2.2.2. Untargeted Analysis

In addition to the targeted screening, a non-targeted GC-HRMS approach was employed to comprehensively explore the chemical complexity of the *Satureja montana* aqueous extract and to identify additional constituents potentially involved in the green synthesis and surface functionalization of microparticles. This strategy aimed to complement the targeted dataset by detecting molecules not included in the calibration mixture but potentially relevant in mechanistic or functional terms.

Following peak deconvolution, a total of 643 individual features were detected. After procedural blank subtraction and spectral quality filtering (Total Score > 90), 169 compounds were identified with high confidence. These were subsequently categorized into major chemical families based on their molecular structures and functional groups. As shown in **Figure 5**, alcohols (22.6%), aromatic hydrocarbons (17.3%), and ketones (8.9%) were among the most represented classes. Esters, polycyclic aromatic hydrocarbons, monoterpenes, and furan derivatives were also identified, while a substantial fraction (34.5%) fell under the category "Others," encompassing structurally ambiguous, multifunctional, or less-characterized phytochemicals. These results provide a broad overview of the chemical landscape of the extract and highlight its richness in oxygenated and aromatic species, which are likely to influence its reactivity and interaction with inorganic surfaces.

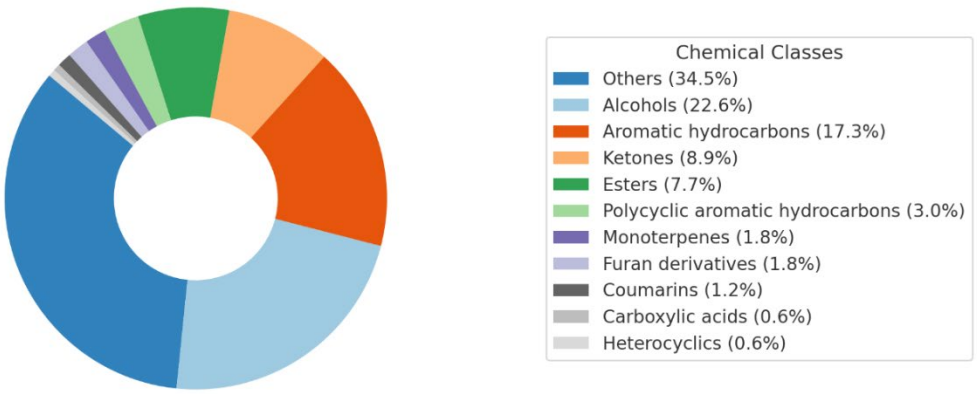

Figure 5. Chemical classification of high-confidence compounds identified in the untargeted GC-HRMS analysis of *Satureja montana* aqueous extract. The chart is based on the compound list reported in **Supplementary Table S1**, where molecules were grouped into chemical families according to their molecular structures and functional groups.

 doi:10.20944/preprints202508.0473.v1

The full dataset, including retention times, average peak areas, molecular formulas, exact and theoretical masses, and NIST match scores, is reported in Supplementary **Table S1**. In many cases, compounds were detected at multiple retention times but shared the same molecular formula and theoretical mass. These signals, retained in the final table, likely represent structural or conformational isomers and are discussed collectively based on their elemental identity.

To focus the discussion on the most relevant compounds, the 22 molecules with the highest peak areas—each with a Total Score > 95 and a Peak Rating > 7.5—were selected and visualized in **Figure 6**. For clarity, thymol and endo-borneol, although confirmed as major constituents, were excluded from the graph due to their disproportionately high abundance, which would distort the scale. Their identity is confirmed and discussed elsewhere in the text.

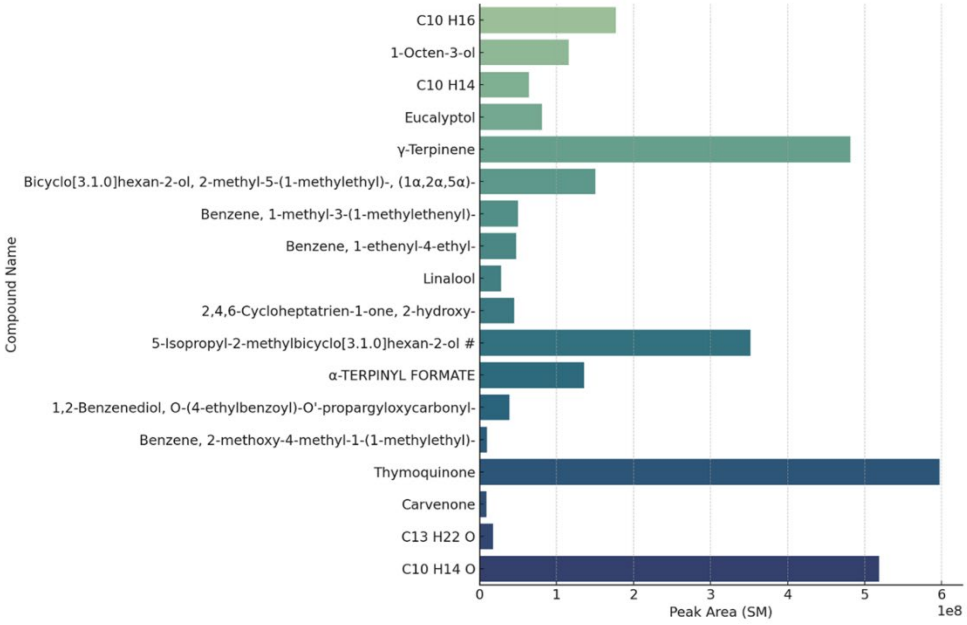

Figure 6. Histogram plot of the 22 most abundant compounds identified in the SM extract based on peak area, ordered by retention time. Thymol and endo-borneol were excluded from the graph due to their disproportionately high peak areas, which would distort the scale. Since it's a single sample, there's no standard deviation. The bars indicate the relative abundance of the compounds in the sample because they are chromatographic peak areas, not quantities.

The selected compounds span a broad retention time range and include molecules with well-defined structure as well as entries reported solely by molecular formula (e.g., $C_{10}H_{16}$, $C_{10}H_{14}$, $C_{13}H_{22}O$). These formula-based entries indicate the detection of multiple peaks with identical mass and elemental composition but distinct chromatographic behaviors, suggesting the presence of unresolved isomeric species. Although further structural elucidation is needed, such components are retained for their potential contribution to the extract's reactivity and its role in downstream applications.

In the following paragraphs, the results regarding the application of TiO_2 MPs/SM and $CaCO_3$ MPs/SM in bacterial cultures are described, and the order of presentation will respect that followed for all other results previously shown.

2.3. Antimicrobial Screening

In the present study, the antimicrobial activity of TiO_2 and $CaCO_3$ MPs was evaluated within an indoor environmental setting. Passive sedimentation method was employed, as this approach is widely regarded as one of the most cost-effective, standardized, and reproducible methods for such investigation [100] The antimicrobial activity of TiO_2 microparticles (MPs) and TiO_2 MPs

 doi:10.20944/preprints202508.0473.v1

functionalized with *S. montana* leaf extract (TiO_2 MPs/SM) was evaluated in comparison with the untreated control (CT) (**Figure 7A**). In the control condition, passive air sampling yielded 66.33 ± 5.51 CFU/plate, representing the baseline microbial load in the indoor environment. When TiO_2 MPs/SM were applied, low to moderate concentrations (0.2–4 mg/mL) produced a statistically non-significant increase in CFU compared to the control, indicating a limited impact on microbial deposition. However, at 10 mg/mL a statistically significant increase was observed 1132.00 ± 46.13 ($p < 0.0001$), and at the highest concentrations (20–50 mg/mL) the number of CFU was found to be too numerous to count (TNTC), suggesting an unexpected promotion of microbial accumulation rather than inhibition. A similar but more pronounced trend was observed for TiO_2 MPs, where even the lowest dose (0.2 mg/mL) caused a dramatic increase in microbial growth 1776.00 ± 166.40 CFU/plate ($p < 0.0001$), further escalating at 2 mg/mL (2785.00 ± 190.31 CFU/plate), with higher concentrations resulting in TNTC. Compared to the CT, both formulations failed to reduce microbial contamination. Contrary to what was observed with TiO_2 MPs data regarding the efficiency of antibacterial activity, promising results were observed with $CaCO_3$ MPs data shown in **Figure 7B**. Compared to the CT (106.00 ± 13.52 CFU/plate), the application of $CaCO_3$ MPs and $CaCO_3$ MPs/SM induced a dose-dependent modulation of microbial growth.

For $CaCO_3$ MPs/SM, low concentrations (0.2–2 mg/mL) did not significantly differ from the control, maintaining CFU counts close to CT, respectively of 102.00 ± 2.00 and 97 ± 1.73 CFU/plate. However, starting from 4 mg/mL, a statistically significant reduction was observed with a value of 75.32 ± 16.04 CFU/plate ($p < 0.01$), which became even more pronounced at 10 mg/mL with a total number of CFU per plate equal 55.67 ± 9.01 CFU/plate ($p < 0.0001$). At 20 mg/mL and 50 mg/mL, microbial growth was almost completely suppressed showing values equal to respectively 6.33 ± 4.04 and 1 ± 1 CFU/plate ($p < 0.0001$), indicating a strong antimicrobial effect at high doses. In contrast, the application of $CaCO_3$ MPs did not produce statistically significant reductions compared to CT at any tested concentration, with CFU counts ranging from 111.70 ± 7.23 at 0.2 mg/mL to 96.00 ± 5.29 at 50 mg/mL, thus remaining within the same range registered for CT.

 doi:10.20944/preprints202508.0473.v1

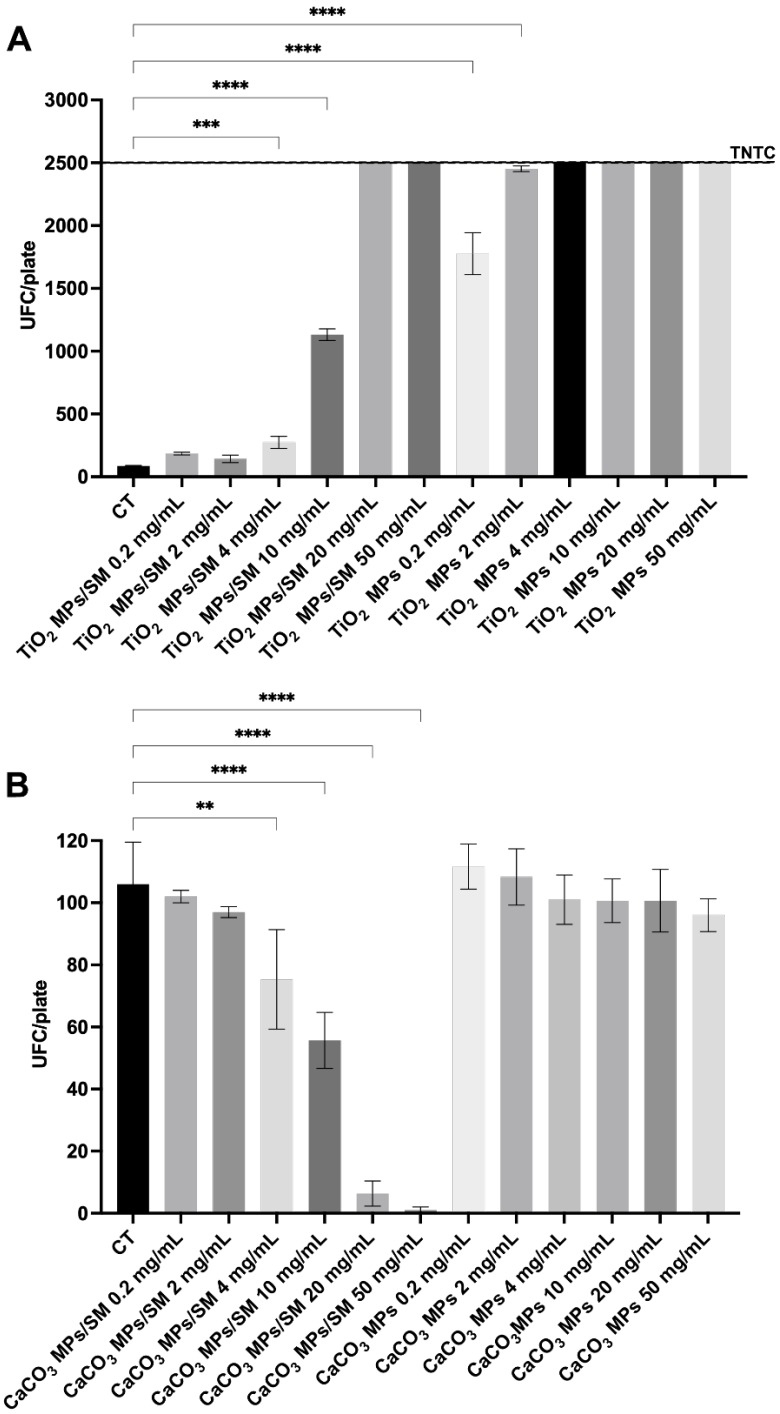

Figure 7. Mean ± SD (n=6) of CFU/plate following passive sedimentation method under different TiO_2 (**A**) and $CaCO_3$ MPs (**B**) treatments. TNTC: Too Numerous To Count (CFU>2500); CT: untreated control. Statistical significance relative to the untreated control is indicated by asterisks: * $p<0.05$; ** $p<0.005$; *** $p<0.001$; **** $p<0.0001$.

Results are also summarized on **Table 4**.

 doi:10.20944/preprints202508.0473.v1

Table 4. Mean ± SD (n=6) of CFU/plate following passive sedimentation method under different TiO_2 and $CaCO_3$ MPs treatments. CT: untreated control. Statistical significance relative to the untreated control is indicated by asterisks: * p<0.05; ** p<0.005; *** p<0.001; **** p<0.0001.

Treatment	Concentration (mg/mL)	CFU/plate	MPs Size _SEM (nm/μm)
Titanium Oxide			
CT	-	86.00 ± 3.60	Diameters ranging from 160 nm to 1.3 μm, with a prevalence of elements with diameters around 400-600 nm
TiO_2 MPs/SM	0.2	184.00 ± 10.58	
	2	142.40 ± 29.70	
	4	274.00 ± 47.62 ***	
	10	1132.00 ± 46.13 ****	
	20	>2500	
	50	>2500	
TiO_2 MPs	0.2	1776.00 ± 166.40 ****	
	2	2452.00 ± 22.27 ****	
	4	>2500	
	10	>2500	
	20	>2500	
	50	>2500	
Calcium Carbonate			
CT	-	106.00 ± 13.53	$CaCO_3$ particles have prismatic shape, sharp edges and variable size, with an average of 1 μm x 1 μm x 1 μm
$CaCO_3$ MPs/SM	0.2	102.00 ± 2.00	
	2	97.00 ± 1.73	
	4	75.33 ± 16.04 **	
	10	55.67 ± 9.02 ****	
	20	6.33 ± 4.04 ****	
	50	1.00 ± 1.00 ****	
$CaCO_3$ MPs	0.2	111.7 ± 7.23	
	2	108.3 ± 9.07	
	4	101.00 ± 7.93	
	10	100.70 ± 7.02	
	20	100.70 ± 10.07	
	50	96.00 ± 5.29	

The data presented in the table clearly demonstrate contrasting antimicrobial behaviours between TiO_2 and $CaCO_3$-based microparticles (MPs), particularly when functionalized with Satureja montana (SM) extract. TiO_2 MPs, both in their pristine (as prepared) and SM-functionalized forms, not only failed to reduce microbial contamination but exhibited a dose-dependent increase in colony-forming units (CFUs), with values exceeding the countable limit (>2500 CFU/plate) at concentrations ≥4 mg mL^{-1}. This suggests a possible aggregation or nutrient-like effect that supports microbial proliferation and cell growth. Instead, $CaCO_3$ MPs/SM showed a clear dose-dependent reduction in microbial load, with statistically significant decreases in CFUs starting from 4 mg mL^{-1} and nearly complete inhibition at higher doses (20–50 mg mL^{-1}). All this finds a reasonable and valid explanation in many factors (undoubtedly regulated by the activators/phase controllers) such as the shape/morphology of the particles, their size, the presence of chemically reactive defects, potentially capable of developing ROS (main inhibitors of cell growth).

Especially, the photocatalytic activity of TiO_2 microparticles is mainly determined by their crystalline phases (anatase has the highest photocatalytic activity), grain size, specific surface area, pore structure, crystallinity, defects, and edges, [100]. The spherical microparticles characterized in this study have dimensions greater than 100 nm (between 400 and 600 nm), are completely smooth and without edges (see the SEM micrographs on **Figure 1**). They do not exhibit significant roughness, as shown by the BET data (see **Table S3** in Supplementary Information), both in terms of porosity

 doi:10.20944/preprints202508.0473.v1

(pore volume 0.0023 cm^3/g; pore size of 560 nm as macropores, according to the International Union of Pure and Applied Chemistry, IUPAC [101]), and surface area (1.20 m^2/g). Furthermore, TiO_2 MPs/SM particles possess carbonyl groups, such as aldehydes and ketones (see the well-defined FTIR signal cantered around 1630 cm^{-1}) that do not have the same rate of oxygen radical-ROS production, when compared to carboxyl groups; C(=O)O-H, which upon oxidative decarboxylation (and other radical-mediated processes) tend to release ROS radicals [64]. Low to moderate ROS levels can act as signaling molecules, promoting cell survival, proliferation, and even resistance to certain therapies [65]. Low reactive oxygen species (ROS) levels can indeed stimulate cell proliferation and inhibit apoptosis, as highlighted on **Figure 7A**.

These functional groups characterized by FTIR are molecular activators/phase controllers, whose role in the synthesis of inorganic particles depends on many parameters, such as: the nature of the inorganic precursor, the type of synthesis performed, the nature of the selected plants, the different concentrations of the activators/phase controllers in the different plants used, the derivatives of the latter employed, i.e., aqueous and/or hydroalcoholic extracts, essential oils and finally exudates. In accordance with what was previously stated, we modified the synthesis temperature (as reported in Supplementary Information, working at lower temperature see Scheme S1) to obtain a brookite/anatase heterophase which, as known from the literature [102], could exhibit superior photocatalytic and antimicrobial activities (for several cases of study, as reported in [102]. Unfortunately, under our working conditions (see Supplementary Information), even the mixed brookite/anatase phase did not show significant antimicrobial activity and therefore future studies will be necessary to improve and optimize the green synthesis with regard to TiO_2 particles in all its crystalline phases (homogeneous and/or mixed phases/heterophases), considering the crucial role exhibited by the natural plants phase controllers/molecular activators.

The results obtained in this study have been compared with those reported in very recent literature (current year 2025 and beyond), all summarized in **Table 5**, where the following considerations could be highlighted:

- anatase and rutile films with the same dimensions (600 nm and grain size of 100 nm; surface area of 1.35 m^2/g) and different shape/morphology as a film, exhibit photodynamic antimicrobial chemotherapy activity against methicillin-resistant Staphylococcus aureus [101]. Only one case of amorphous TiO_2 spheres, with larger dimensions (φ=2000 nm and surface area of 0.85 m^2/g) still shows antimicrobial activity (as reported on **Table 5**).

- in all other case studies, involving mesoporous TiO_2 ($3 \leq \varphi < 50$ nm) with higher surface area (ranging from 60 to 36 m^2/g), statistically significant antibacterial, antimicrobial and antioxidant activities are still present (see **Table 5** and all the references reported therein).

Table 5. All the characterization parameters for TiO_2 MPs/SM. **B**: Brookite; **A**: Anatase; **R**: Rutile in the text.

Samples	SEM (φ: nm) Shape	XRD 2θ (plane)	Raman cm^{-1} (mode)	SM extract composition (GC-MS)	References	Notes
TiO_2 MPs/SM	400 – 600 nm μ-Spheres	11.74° (101)/A 17.45° (112)/A 21.77° (200)/A 24.60° (211)/A 27.91° (204)/A 30.54° (220)/A 32.90° (301)/A	(146, 219, 623) E_g/A (411, 517) B_{1g}/A (517) A_{1g}/A (219) B_{1g}/B (279) B_{2g}/B	α-Thujone α-pinene Camphene Sabinene β-Pinene α-Phellandrene alfaTerpinene para-cymene (R)-(+)-Limonene α-Terpinolene γ-Terpinene Terpinen 4-ol Carvacrol methyl ether	This work (**2025**)	No antimicrobial performances have been observed

 doi:10.20944/preprints202508.0473.v1

		35.63° (312)/A 11.74° (111) /B 21.77° (231)/B		L-Carvone Thymoquinone Geraniol Thymol Carvacrol β-Caryophyllene α-Humulene caryophyllene oxide cis-α-bisabolene (Levomenol) L-Linalool		
Anatase and rutile ***film***	600 nm size, grain size: 100 nm film	The anatase films appear as flat terraces with mono-atomic steps. The 'grains' have a slightly rectangular shape and two kinds of rectangular grains oriented 90 to each other are observed. These are due to the before mentioned twinning of the films	Not reported in the text	Not reported in the text	[101]	Photodynamic antimicrobial chemotherapy activity against Methicillin resistance Staphylococcus aureus
TiO_2 NPs/ *clove extract*	19-33 nm Spheres	Not reported	Not reported	Not reported for the clove extract	[102]	Alcohol-based clove extract combined with TiO_2 nanoparticles is a potent antimicrobial agent, capable of inhibiting VMRSA growth even at low concentrations
TiO_2 NPs from Sigma Aldrich (Saint Louis, MO, USA) Loaded with	21 nm (as reported by Sigma	Not reported in the article, where commercial	Not reported in the article, where commercially available	Not reported for the Polygonum cuspidatum Extract	[103]	Incorporating *P. cuspidatum* root extract into TiO_2 nanoparticles

 doi:10.20944/preprints202508.0473.v1

Polygonum cuspidatum Extract	Aldrich) Spheres	ly available nanoparticles have been applied	nanoparticles have been applied			significantly enhances their antioxidant and hemocompatibility properties. TiO_2-loaded extract NPs exhibited excellent antibacterial properties against the tested strains
Green synthesis TiO_2 nanoparticles using *Sophora flavescens* root extract	8-24 nm Spheres	(100) A (004) A (204) A (105) A (211) A (204) A	Not reported only FTIR	Not reported for the *Sophora flavescens* root extract	[104]	Their stability and ability to penetrate bacteria cells enhance their antibacterial efficacy, particularly against gram-positive bacteria
TiO_2 nanoparticles were synthesized using *Talinum fruticosum* leaf extract	3-12 nm Spheres	24.92° (101) A 68.99° (200) R	Not reported only FTIR	Not reported for the *Talinum fruticosum* leaf extract	[105]	TiO_2 showed photocatalytic activity and anti-inflammatory property as the protein degradation inhibition capacity
TiO_2 P25 TiO_2 Br200	mean diameter of 40 nm 10-15 nm	79 % anatase/A 21% rutile/R 45% anatase/A 2% rutile/R 53% brookite/B	Not reported	No plant extract was applied for the synthesis of these nanoparticles	[106]	Biphasic brookite-anatase nanoparticles, due to their smaller particle size, may increase the efficiency of TiO_2 nanoparticles to inhibit bacterial growth by promoting a greater surface area contact ratio
	2000 nm amorphous	Degussa P25 (80% anatase	(144, 196, 639 cm^{-1}) E_g/A	TiO_2 without functionalization	[107]	The bactericidal activity and

 doi:10.20944/preprints202508.0473.v1

TiO_2, anatase, brookite and rutile, have been synthetized through a microwave-assisted hydrothermal method using amorphous TiO_2 as a common precursor	(spheres) 15 nm A (spheres) 20 nm Degussa P25 (spheres) 20 nm B (spheres) 20 nm R rod-shaped	and 20% rutile), A (100% purity) B (94% purity) R (100% purity)	(399, 519 cm^{-1}) B_{1g}/A (513 cm^{-1}) /A (127, 154, 194, 247, 412, 640 cm^{-1}), A_{1g}/B (133, 159, 215, 320, 415, 502 cm^{-1}) B_{1g}/B (235, 450 cm^{-1}) /R	, as reported in the full text	photocatalytic antibacterial effectiveness of each material were evaluated through the determination of the minimum inhibitory and bactericidal concentrations, and via the mortality kinetic method under ultraviolet (UV) illumination under similar conditions with two bacterial groups of unique cellular structures: Gram-negative Escherichia coli (E. coli) and Gram-positive Staphylococcus aureus (S. aureus).

Degussa P25: selected samples of the amorphous TiO_2, a reference sample of Degussa P25 (80% anatase and 20% rutile), commercially available, as reported in the ref. [108].

A different trend (in terms of antimicrobial features, see **Figure 7B**) was obtained in presence of porous micrometric $CaCO_3$ MPs/SM prismatic particles (see SEM micrographs on **Figure 3** and BET data on **Table S3**. in Supplementary Section). The phase controllers/activators induce (during the nucleation and growth of calcite particles) lattice defects, such as vacancies or dislocations, that represent irregularities in the material structure. These defects can act as active sites for chemical reactions (i.e., oxidation, reduction, hydrolysis, etc.;) or alter the electronic structure of the materials [108]. The edges of material structures offer a higher density of reactive sites compared to the basal plane [109] by favouring/promoting the formation of C(=O)OH carboxylic groups, the main sources of ROS, that induce growth inhibition of microorganisms (as clearly highlighted on Figure 7B, in the text). These results are also compared with the most recent literature reported on **Table 6**, where it is possible to note how calcite nanoparticles, synthesized with different eco-sustainable approaches and equipped with different shapes, size and roughness can induce antimicrobial, antibacterial, antioxidant effects on selected bacterial cultures and strains, thanks to the presence of chemically reactive sites such as carboxylic groups (mainly C(=O)-OH), (see references cited into **Table 6**). The higher density of oxygenated functional groups on the structural defects and edges, also provides to

 doi:10.20944/preprints202508.0473.v1

$CaCO_3$ MPs/SM with prismatic shape and micrometric size, a Z potential value equal to -25.14 mV due to the acidic dissociation of carboxylic groups C(=O)OH/into carboxylate (C=(O)O$^-$)) anions and phenols/into phenoxide or phenate anion, the latter more acidic than aliphatic alcohols at the working pH (pH=6.6 in bidistilled water, as working medium). These reactive functional groups were also quantified through the volumetric titration of the acidic sites, as reported in literature [110]. The carboxyl groups quantified on the $CaCO_3$ MPs/SM particles were found to be equal to 41.31 nmol/mg (while those on the TiO_2 MPs/SM spherical particles were found to be equal to 14.66 nmol/mg, in comparison), see also Table S4 on Supplementary text. Furthermore, particles with a negative Zeta-potential value (see **Table S4** in Supporting information), on the other hand, could be attracted to the positively charged bacterial cell surface (especially *Staphylococcus aureus* as a valuable Gram-positive bacterial model) through electrostatic interactions, facilitating their attachment and potentially disrupting the cell membrane.

Finally, we have not included in this manuscript the VP-SEM observations of the bacterial cultures used for the analyses presented in this work, this because such ultrastructural morphological analysis requires the development of a specific protocol. We are therefore developing an experimental model that will allow us to observe, using VP-SEM, the effect of TiO_2 and $CaCO_3$ administration on bacterial cultures. Once the optimal experimental conditions have been established, we will conduct the morphological analysis to confirm the effect of crystal shape on bacterial growth capacity (for detail of the experimental model we are developing, Supplementary Material Section).

Table 6. All the characterization parameters for $CaCO_3$ MPs/SM. **C**: calcite/$CaCO_3$.

Samples	SEM (φ: nm) Shape	XRD 2θ (plane)	Raman cm^{-1} (mode)	SM extract composition (GC-MS)	References	Notes
$CaCO_3$ MPs/SM	1 μm x 1 μm x 1 μm Prismatic shape	29.43° (104) /C 31.46° /C 56.54° /C 58.20° /C	248 cm^{-1} (E_g) C lattice 718 cm^{-1} (E_g) C 1092 cm^{-1} (A_{1g}) C	α-Thujone α-pinene Camphene Sabinene β-Pinene α-Phellandrene alfaTerpinene para-cymene (R)-(+)-Limonene α-Terpinolene γ-Terpinene Terpinen 4-ol Carvacrol methyl ether L-Carvone Thymoquinone Geraniol Thymol Carvacrol β-Caryophyllene α-Humulene caryophyllene oxide cis-α-bisabolene (Levomenol) L-Linalool	This work (**2025**)	$CaCO_3$ MPs/SM exhibit antimicrobial properties, depending on the particle concentrations, shape, defects, edges, dislocations and density of oxygenated functionalities on edges
Hollow calcium carbonate microsphere	1.97 ± 0.61 μm	XRD analysis of the $CaCO_3$ hollow	Not reported in the text	Not reported in the text for the carvacrol loading	[111]	The antimicrobial results indicated that

 doi:10.20944/preprints202508.0473.v1

s loaded by carvacrol	hollow microsphe res	microsphe res revealed that they are primarily aragonite (standard card: JCPDS#33–0268)				microSCaCA effectively inhibited and killed E. coli and S. aureus, markedly enhancing the efficacy of CA, and exhibiting cellular safety. In practical preservation applications, microSCaCA significantly improved the preservation of pork during 4 ◦C storage, inhibiting key indicators such as TVB-N, pH, TBARS, and TVC, effectively delaying the oxidation of fats and proteins and suppressing the growth of microorganis ms during the storage period
$CaCO_3$ nanoparticle s have been synthetized by using dried powder of mollusc shells	60-70 nm spheres	23.1◦ (012) 29.3◦ (104) 31.4° (006) 35.9◦ (110) 39.4◦ (113) 42.7◦ (202) 47.5◦ (018) 48.5◦ (116) 57.4◦ (122) 60.7◦ (214) 64.4◦ (300) 65.4◦ (0012) (JCPDS No. 85–1108)	Not reported in the text but only FTIR	The synthesis of calcium carbonate nanoparticles from mollusk shell waste occurred without any natural plant extracts. Therefore, this characterization is not specifically contemplated in the text.	[112]	A low level of oxidative stress was recorded under all treatments of $CaCO_3$NPs, and the highest decrease in MDA and $O_2^{\bullet-}$ contents of about 12 % and 23 % were recorded under 30 mg/L of $CaCO_3$NPs

 doi:10.20944/preprints202508.0473.v1

						compared to the control, respectively. The antioxidant system was improved under $CaCO_3$NPs treatments and the highest increase of about 22 % and 37 % in CAT and SOD activity were recorded at 30 mg/L of $CaCO_3$NPs compared to the control, respectively.
The extract of Hyphaene thebaica L. Mart (Egyptian doum palm) fruits was used as the reducing/capping agent for the synthesis of $CaCO_3$ nanoparticles	60 nm - 180 nm shapes from quasi-spherical, to cubical with equiaxed morphology	012 104 110 113 202, 018, 116 211 122 214 300 correspond to the rhombohedral calcite phase of $CaCO_3$, which is following with the X-pert standard card #47–1743	Not reported in the text but only FTIR	Not reported in the text for the extract of Hyphaene thebaica L. Mart (Egyptian doum palm) fruits	[113]	$CaCO_3$ NPs exhibit antifungal activity and therefore, the findings of this study suggest that the inclusion of a green synthesis of $CaCO_3$ NPs as a nonfertilizer has the potential to promote tomato growth and yield.
The extract of Hyphaene thebaica L. Mart (Egyptian doum palm) fruits was used as the reducing/ca	60 nm - 180 nm shapes from quasi-spherical, to cubical with	012 104 110 113 202, 018, 116 211 122 214	Not reported	Not reported for the extract of Hyphaene thebaica L. Mart (Egyptian doum palm) fruits. This investigation has been reported only for the metabolomes of both tomato cultivars (Heinz-	[114]	The application of $CaCO_3$NPs increased the presence of terpenoids and flavonoids in both fruits and leaves compared

 doi:10.20944/preprints202508.0473.v1

pping agent for the synthesis of $CaCO_3$ nanoparticles	equiaxed morphology	300 correspond to the rhombohedral calcite phase of $CaCO_3$, which is following with the X-pert standard card #47–1743	1370andMoneymaker), before and after $CaCO_3$ NPs inoculation/treatments.	with the untreated plants. Metabolites such as 13-hydroxy abscisic acid, Dantaxusin A, and Sinuatol were identified in the leaves of the Moneymaker cultivar, with 30-O-linolenoylglyceryl6-O-galactopyranosyl-galactopyranoside, Olean-12-en-28-oic acid and scutianthraquinone B present in the fruits.

3. Materials and Methods

In accordance with what reported above for the results and their discussion, also the experimental part will follow the same order of presentation, that is: materials/measurement procedures for the synthesis and characterization of microparticles and natural extracts from SM; in the second part the materials/measurement procedures for the characterization of the antibacterial, antimicrobial, anti-oxidant, anti-biofilm properties of microparticles functionalized with natural extracts of SM, will be described, respectively.

3.1. Plant Materials and Chemicals/Reagents

SM plants (*Satureja montana L.*, *Lamiaceae*, commonly known as winter savory) were collected from Orto Botanico di Roma Sapienza University (Italy), during the flowering phase (on July 2024), where the term of harvest had a significant effect on the chemical content of Essential Oils and Natural Extracts in *Satureja montana* [115]. Each plant during the sampling step was hand-harvested into Ziploc storage containers and transported to the laboratory. Leaves were manually removed and let it dry at room temperature and under pressure for two weeks until extraction.

All Chemical reagents are of analytical grade and purchased from Merck (Germany), including Titanium Tetra Isopropoxide (TTIP, $C_{12}H_{28}O_4Ti$, 97%), ethanol (C_2H_5OH, 96%), n-hexane (C_6H_{14}, 98.5%), and the following GC-MS standards: α-humulene ($C_{15}H_{24}$, 90%), α-phellandrene ($C_{10}H_{16}$, 85%), α-pinene ($C_{10}H_{16}$, 98%), α-terpinolene ($C_{10}H_{16}$, 95%), aromadendrene oxide 2 ($C_{15}H_{24}O$, 95%), β-caryophyllene ($C_{15}H_{24}$, 80%), β-myrcene ($C_{10}H_{16}$, 90%), β-pinene ($C_{10}H_{16}$, 99%), carvacrol ($C_{10}H_{14}O$, 98%), carvacrol methyl ether ($C_{11}H_{16}O$, 90%), caryophyllene oxide ($C_{15}H_{24}O$, 98%), *cis*-α-bisabolene ($C_{15}H_{24}$, 93%), *cis*-sabinene hydrate ($C_{10}H_{18}O$, 97%), D-carvone ($C_{10}H_{14}O$, 98%), geraniol ($C_{10}H_{18}O$, 98%), (R)-(+)-limonene ($C_{10}H_{16}$, 97%), γ-terpinene ($C_{10}H_{16}$, 95%), L-linalool ($C_{10}H_{18}O$, 95%), *para*-cymene ($C_{10}H_{14}$, 99%), sabinene ($C_{10}H_{16}$, 75%), (+)-terpinen-4-ol ($C_{10}H_{18}O$, 98%), and thymol ($C_{10}H_{14}O$, 99%). Other used chemicals and solvents were of the highest analytical grade, as perdeuterated

 doi:10.20944/preprints202508.0473.v1

fluoranthene (Chemical Research 2000 S.r.l., Milan, Italy) and NaCl (Merck, Germany). Bidistilled water is obtained with the Millipore system (Milli-Q® EQ 7000) and all aqueous and/or hydroalcoholic solutions are freshly prepared every day, to carry out all the measurements.

3.2. Preparation of TiO_2 Microparticles in SM' Natural Extracts (TiO_2 MPs/SM)

SM' natural extracts were obtained by drying the leaves of the plants (3 plants). These latter were harvested, dried, and subsequently ground using a mortar. To prepare the extract, 2 g of the pulverized leaves were immersed in 60 mL of bidistilled water and heated to 40°C under continuous stirring for 1 hour. The resulting extract was filtered, cooled to room temperature and stored in a dark glass bottle at 4°C. This protocol agrees with the literature [116], but we have modified it for the aqueous (and not organic) solvent and for the thermal treatment at lower temperature.

TiO_2 particles were synthesized starting from Titanium Isopropoxide (TTIP, used here as titanium oxides precursor) in ethanol as working medium, according to the literature [117]. Briefly, 5 mL of TTIP is dissolved in 5 ml of ethanol solution and 2 mL of aqueous SM's extract (added drop by drop into the reaction environment), under continuous stirring for 3 hours at Room Temperature (RT). The solid was vacuum filtered, washed thoroughly with 250 mL of double-distilled water, and finally dried in an oven at 60°C (without calcination step, which is known to occur at temperatures well above that used in this study). The resulting TiO_2 MPs/SM were collected and processed with further characterization measurements.

3.3. Preparation of $CaCO_3$ Microparticles in SM' Natural Extracts ($CaCO_3$ MPs/SM)

SM' natural extracts were obtained according to the previous paragraph. $CaCO_3$ particles were synthesized starting from calcium chloride ($CaCl_2$) and sodium carbonate (Na_2CO_3) used here as precursor, according to the literature [118,119]. Briefly, 200 ml of 50mM $CaCl_2$ and 50 ml of aqueous SM's extract were mixed together under magnetic stirring at 400 rpm for 5 min (at R.T.). Then, 250 ml of 50 mM Na_2CO_3 was added to the previous solution, which is left under magnetic stirring at 400 rpm for 15 min (at R.T.). The solid was vacuum filtered, washed thoroughly with 250 mL of double-distilled water, and finally dried in an oven at 60°C. The resulting $CaCO_3$ MPs/SM were collected and processed with further characterization measurements.

3.4. (TiO_2 MPs/SM) and ($CaCO_3$ MPs/SM) Characterization Study

In this paragraph, the order of presentation of the measuring apparatus and experimental procedures performed will follow the one adopted previously in the text, for the presentation of the experimental results.

3.4.1. SEM/EDX

The method is the same for both $CaCO_3$ microparticles and TiO_2 microparticles. An ethanol-based (100%) suspension containing a small amount of microparticles was prepared in a glass tube and exposed to one hour of sonication. Upon completion, 10 µL of the suspension was rapidly drop-cast onto 200 mesh copper grids coated with Formvar film (Ted Pella, USA). These grids were then set atop absorbent paper inside a Petri dish, covered, and left to dry under ambient conditions. Once the grids were fully dried, they were mounted onto aluminum stubs using carbon tape and introduced into a sputter coater (Emitec K550, Emitech Corato, Italy), where they were coated with platinum at a current of 15 mA for 1.5 minutes. This sputtering process was conducted twice to ensure uniform coating. For the Scanning Electron Microscopy and image analysis, samples were examined using a Variable Pressure Scanning Electron Microscope (VP-SEM), specifically the Hitachi SU3500 model (Hitachi, Tokyo, Japan), operated under high vacuum conditions at an accelerating voltage of 15–20 kV [120–122]. This SEM system is equipped with dual energy-dispersive X-ray spectroscopy (dEDS) detectors (Bruker XFlash® 6|60), enabling simultaneous multimodal imaging and spatially resolved chemical mapping. This advanced analytical capability is particularly effective for

 doi:10.20944/preprints202508.0473.v1

investigating biological surfaces in their native state. The XFlash® 6|60 is well-suited for nanoanalytical applications involving materials with relatively low X-ray emission [117,118]. For the image analysis, the SEM micrographs were collected using Hitachi Map 3D software, version 8.2 (Digital Surf, Besançon, France) [123,124].

3.4.2. XRD

Powder X-ray diffraction (PXRD) analyses were carried out using a Rigaku SmartLab SE powder diffractometer (Rigaku, Tokyo, Japan), operating with a Cu Kα radiation anode at 40 kV and 30 mA, and equipped with a Rigaku D/teX Ultra 250 silicon strip detector. As the instrument is designed for powder analysis, samples were analyzed directly, without any additional preparation. To improve peak resolution in the high-angle region and to detect weaker diffraction signals, a second set of PXRD measurements was acquired using a D8 Advance diffractometer (Bruker, Billerica, MA, USA) equipped with a Mo Kα radiation source. The use of a shorter X-ray wavelength enabled the detection of additional reflections that were not clearly resolved under Cu Kα irradiation.

3.4.3. Raman Spectroscopy

Samples were analysed using a micro-Raman system equipped with a Cobolt 08-DPL 532 nm solid-state laser (Cobolt AB, Solna, Sweden), coupled with an HRS500 spectrometer (Teledyne Princeton Instruments, Trenton, NJ, USA) with a 50 cm focal length, and a 100× objective (NA = 0.9, model MPLFLN100XBD, Olympus Corporation, Tokyo, Japan), ensuring high spatial resolution. All spectra were collected directly on the microparticle powders without specific sample preparation.

3.4.4. FTIR Spectroscopy

The Fourier Transform Infrared spectroscopy (FTIR) measurements were performed in attenuated total reflection (ATR) mode. A Nicolet Summit FTIR spectrometer (Thermo Fisher Scientific Inc., Waltham, MA, USA), equipped with an Everest™ Diamond ATR accessory (Thermo Fisher Scientific Inc., Waltham, MA, USA), was used. Spectra were acquired with the following parameters: 32 scans per sample, a resolution of 8 cm^{-1}, and a spectral range of 4000–600 cm^{-1}. As the analysis was performed using FTIR in ATR mode, the powdered samples were analyzed by placing them directly in contact with the diamond crystal, without any prior preparation.

3.4.5. GC-MS Analysis of SM Extract: Molecular Composition

The chemical composition of the aqueous extracts obtained from *Satureja montana* leaves was investigated using an untargeted approach based on gas chromatography coupled with high-resolution Orbitrap mass spectrometry (GC-HRMS). The analyses were performed on a Thermo Scientific™ system operated in full scan mode, with a resolving power of up to 50,000 FWHM at m/z 272 and mass accuracy below 1 ppm.

Headspace solid-phase microextraction (HS-SPME) was performed using a Tri Plus RSH autosampler (Thermo Fisher Scientific Inc., Waltham, MA, USA) coupled with an 80 µm thick, 10 mm long multi-adsorbent DVB/CarbonWR/PDMS fiber (Supelco, Merck KGaA, Darmstadt, Germany). The fiber was initially conditioned at 280°C for 60 minutes. For all samples, the fiber was pre-conditioned for 5 minutes at 270°C and post-conditioned for 3 minutes at 270°C after injection. Headspace extraction of samples was carried out in 20 mL vials containing 2 g of NaCl, previously dried at 300°C for 4 hours. To these vials, 10 mL of sample were added, spiked with 20 ng of perdeuterated fluoranthene (Chemical Research 2000 S.r.l., Milan, Italy) as an internal standard. Each vial was conditioned at 70°C for 25 minutes prior to fiber sampling. The SPME fiber was exposed to the headspace vapors for 10 minutes under agitation at 5 revolutions/minute. The SPME needle penetrated the vial by 40 mm, ensuring the full 10 mm length of the fiber was exposed. Subsequently, the fiber was desorbed for 5 minutes at 270°C in a split/splitless injector in split mode (1:50).

 doi:10.20944/preprints202508.0473.v1

Chromatographic separation was performed using an Rxi-5Sil MS column (30 m x 0.25 mm I.D. x 0.25 μm film thickness; Restek Corporation, Bellefonte, PA, USA), operated under a programmed temperature gradient. The carrier gas was helium 5.5 (Nippon Gases Italia S.r.l., Milan, Italy) at a constant flow rate of 1 mL/min. The GC oven temperature program started at 40°C, held for 5 minutes, then increased at 6°C/min to 150°C, and subsequently at 15°C/min to 280°C, with a final isothermal hold of 3 minutes.

A dedicated analytical batch was designed to ensure reproducibility and background control. This batch included procedural blanks—Milli-Q water and filtered water—processed and analyzed under identical conditions as the SM extract samples. These blanks were used for background subtraction during data processing. Additionally, the batch included a five-point calibration curve of a terpene standard mixture at concentrations of 0.08, 0.20, 1.00, 2.00, and 2.01 ng/μL, to each point of which 20 ng of perdeuterated fluoranthene internal standard was added, enabling semi-quantitative analysis of the identified compounds.

Raw data were processed using Compound Discoverer™ 3.3.3.200 software following a two-step deconvolution workflow. In the first step, all features were extracted and aligned across the dataset, with blank subtraction applied to remove procedural background. In the second step, the same dataset was reprocessed to quantify the analytes by comparing the response intensities against the terpene standard mixture, enabling a semi-quantitative estimation of compound abundance.

Peak detection parameters were configured to ensure robust compound annotation. The mass tolerance was set at 5 ppm, the minimum spectral signal-to-noise ratio at 10, and the minimum chromatographic peak S/N threshold at 3. A total ion current (TIC) threshold of 1,000,000 was applied based on signal intensities observed in real samples. The ion overlap for spectral matching was fixed at 98%, and high-resolution filtering (HRF) scoring was enabled. For compound identification via spectral libraries, both the similarity index (SI) and reverse similarity index (RSI) thresholds were set at 600.

All detected features were filtered for reproducibility across replicates, retention time consistency, and spectral match quality. Confidently identified compounds were grouped into major chemical families, including monoterpenes, sesquiterpenes, diterpenes, phenolic compounds, and long-chain fatty acid derivatives. This comprehensive VOCs fingerprint of *Satureja montana* provided the chemical basis for interpreting the role of the molecular activators/phase controllers during the inorganic particles synthesis.

3.5. Experimental Biological Testing and Sampling

To evaluate the potential antimicrobial properties of TiO_2 and $CaCO_3$ MPs, 500 μL of each solution at the previously specified concentrations were aseptically dispensed onto Petri dishes containing 25 mL of culture medium (Plate Count Agar, Liofilchem). The solution was evenly distributed across the agar surface under sterile conditions to ensure homogeneous coverage, and plates were subsequently used for the sampling phase. The sampling was performed using the passive sedimentation method, which measures the amount of microorganisms settle on surfaces by exposing settle plates to air for a defined period of time [125]. In detail, rather standard 9 cm Petri dishes were used to collect the biological particles as sediments, randomly positioned in a public indoor area of 25 m^2, according to the 1/1/1 scheme (for 1 hour, 1 meter above the floor and about 1 meter away from walls and major obstacles) [126]. For each treatment were used six opened MPs treated Petri dishes and six untreated plates were used as controls (CT). At the end of the exposure period the plates were incubated at a temperature of 25°C for 48 h. Bacterial colonies were manually counted by placing each Petri dish on a gridded plate and enumerating colonies within each cell, and the results are expressed as CFU per plate (CFU/plate).

3.5.1. Statistical Analyses

 doi:10.20944/preprints202508.0473.v1

Statistical analyses were performed using GraphPad Prism 10.1.2 (GraphPad Software Inc., San Diego, USA). Data normality was verified with the Shapiro–Wilk test ($p<0.05$), allowing parametric analysis by ANOVA followed by Tukey's post-hoc test. Significance was set at $p<0.05$.

4. Conclusions

TiO_2/A and $CaCO_3$/C microparticles, modified with the aqueous extract of SM plant in the main form of Anatase (A) and Calcite (C), were synthesized, characterized and tested for their antimicrobial activity. The TiO_2 MPs/SM particles (mainly anatase but also the tested heterophase brookite/anatase) did not show significant antimicrobial activity and exhibited a dose-dependent increase in colony-forming units (CFUs), with values exceeding the countable limit (>2500 CFU/plate) at concentrations ≥4 mg mL^{-1}. This suggests a possible aggregation or nutrient-like effect that supports microbial proliferation and cell growth. A low to moderate level of ROS concentration on the non-porous TiO_2/A microparticles, could be responsible for bacterial proliferation and cell growth. What has been observed experimentally is confirmed by the identification of carbonyl-type chemical defects (aldehyde-ketones, by FTIR), which are less reactive in producing ROS than carboxylic-type functional groups.

Instead, $CaCO_3$ MPs/SM exhibit strong and dose-dependent antimicrobial activities, achieving near-complete inhibition at 50 mg mL^{-1}. Most likely, the same molecular activators/phase controllers, contained in SM plant extracts, in presence of calcite precursors (under the same low temperature conditions), are able to induce the particles growth with morphology (prismatic particles), size, porosity and edges/defects/chemical functionalities responsible for a very evident synergistic inhibitory effect, against the strains of microorganisms used in this study. Especially, chemical reactive defects are identifiable as carboxylic groups (by FTIR spectroscopic analysis, C(=O)-OH), which represent the main source of ROS, able to inhibit the bacterial growth.

In conclusion, the SM aqueous extract used for the first time in the synthesis of calcite and anatase particles (avoiding calcination) is an excellent source of molecular activators/phase controllers, especially in the presence of the $CaCO_3$ MPs/SM precursors.

However, for the TiO_2 MPs/SM anatase particles, the activators/phase controllers did not appear to induce antimicrobial effects. For this case study, it would be advisable to use other plants with higher concentrations of activators/phase controllers; or to experiment with SM essential oils and/or plant exudates, which are much more concentrated than the aqueous extract (used in this work), in terms of oxygenated terpenoids.

Supplementary Materials: The following supporting information can be downloaded at the website of this paper posted on Preprints.org, **File S1**: The full dataset, including retention times, average peak areas, molecular formulas, exact and theoretical masses, and NIST match scores, is reported in Supplementary **Table S1**. **File S2**: The XRD and Raman spectra of mixed sample of brookite (major phase)/anatase (minor phase) are reported on **Figure S1** and **S2,** respectively. On **Table S2**, the Raman assignment bands are also summarized. Raman spectrum of the organic activators/phase controllers into TiO_2 MPs/SM sample, has been also reported on **Figure S3**. **File S3**: The BET porosity data (surface area, pore volume and pore size) are reported on **Table S3**. **File S4**: while the Z-potential /DLS values are reported on **Table S4**. **File S5**: the VP-SEM protocol that will be optimized is reported on **Text S4**. Also, Supplementary References were included.

Author Contributions: Conceptualization, F.V., R.B., F.S., L.R., M.R., and M.R.; methodology, F.V., E.G., R.B., M.R., R. De M., M.R., and I.C.; formal analysis, I.C., L.R, R.R., R. De M., and M.C.; resources, F.V. and A.C.; data curation, I.C., C.Z., M.C; E.G. and M.R.; writing—original draft preparation, F.V., M.R., A.M. and R.B.; writing—review and editing, M.R., M.R., A.M., I.C., and C.Z.; supervision, F.V., A.C. and I.A.; project administration, F.V., I.A.; funding acquisition, F.V and A.C. All authors have read and agreed to the published version of the manuscript.

Funding: This research was supported by a grant for "Economic valorisation of patents in favour of micro, small and medium-sized enterprises", called "Brevetti +" CUP: C85F20000440008), co-financed by the Ministry of

 doi:10.20944/preprints202508.0473.v1

Economic Development. Tor Vergata Brevetti POC-TV.B.POC according to the proof of concepts of the Italian Minister of Economic Development, "Tor Vergata Brevetti Poc—TV.B. Poc", with CUP code C86I20000130004, admitted to financing with communication from the National Agency for Investment Attraction and Business Development S.p.A.—Invitalia prot. no. 0139954 of 09/18/2020 and subsequent financing granting act prot. no. 0175114 of 11/10/2020.

Institutional Review Board Statement: Not applicable.

Informed Consent Statement: Not applicable.

Data Availability Statement: Data are contained within the article.

Acknowledgments: We are grateful to: Roberto Braglia and Antonella Canini for preparing sterile media and plates for the growth of the bacteria and microorganism, and to Massimo Reverberi and Roberto Braglia at the Botanical Garden of Sapienza University and the Botanical Garden of Rome Tor Vergata University, respectively, for helping us identify and harvest the plant materials, and to Ettore Guerriero and Marina Cerasa for the GC-MS analysis and terpenoids identification from extract of *Satureja montana*. The authors would also like to thank Prof. Olga Russina and the CNIS (Center of Nanotechnology for Engineering of Roma Sapienza) of Sapienza University (Rome) for the X-ray diffraction (XRD) measurements. All the authors thank the Department of Physics of the Sapienza University of Rome for the in-depth analysis of Raman signals regarding TiO_2 polymorphs.

Conflicts of Interest: The authors declare no conflicts of interest.

References

1. Patra, A.R.; Pattnaik, A.; Ghosh, P. The Latest Breakthroughs in Green and Hybrid Nanoparticle Synthesis for Multifaceted Environmental Applications. *J Taiwan Inst Chem Eng* **2025**, 106157, doi:10.1016/j.jtice.2025.106157.
2. Pattnaik, A.; Sahu, J.N.; Poonia, A.K.; Ghosh, P. Current Perspective of Nano-Engineered Metal Oxide Based Photocatalysts in Advanced Oxidation Processes for Degradation of Organic Pollutants in Wastewater. *Chemical Engineering Research and Design* **2023**, *190*, 667–686, doi:10.1016/j.cherd.2023.01.014.
3. Suman, T.Y.; Radhika Rajasree, S.R.; Ramkumar, R.; Rajthilak, C.; Perumal, P. The Green Synthesis of Gold Nanoparticles Using an Aqueous Root Extract of Morinda Citrifolia L. *Spectrochim Acta A Mol Biomol Spectrosc* **2014**, *118*, 11–16, doi:10.1016/j.saa.2013.08.066.
4. Velmurugan, P.; Anbalagan, K.; Manosathyadevan, M.; Lee, K.J.; Cho, M.; Lee, S.M.; Park, J.H.; Oh, S.G.; Bang, K.S.; Oh, B.T. Green Synthesis of Silver and Gold Nanoparticles Using Zingiber Officinale Root Extract and Antibacterial Activity of Silver Nanoparticles against Food Pathogens. *Bioprocess Biosyst Eng* **2014**, *37*, 1935–1943, doi:10.1007/s00449-014-1169-6.
5. Behravan, M.; Hossein Panahi, A.; Naghizadeh, A.; Ziaee, M.; Mahdavi, R.; Mirzapour, A. Facile Green Synthesis of Silver Nanoparticles Using Berberis Vulgaris Leaf and Root Aqueous Extract and Its Antibacterial Activity. *Int J Biol Macromol* **2019**, *124*, 148–154, doi:10.1016/j.ijbiomac.2018.11.101.
6. Saeed, S.Y.; Mazhar, K.; Raees, L.; Mukhtiar, A.; Khan, F.; Khan, M. Green Synthesis of Cobalt Oxide Nanoparticles Using Roots Extract of Ziziphus Oxyphylla Edgew Its Characterization and Antibacterial Activity. *Mater Res Express* **2022**, *9*, 105001, doi:10.1088/2053-1591/ac9350.
7. Ganesh Kumar, V.; Dinesh Gokavarapu, S.; Rajeswari, A.; Stalin Dhas, T.; Karthick, V.; Kapadia, Z.; Shrestha, T.; Barathy, I.A.; Roy, A.; Sinha, S. Facile Green Synthesis of Gold Nanoparticles Using Leaf Extract of Antidiabetic Potent Cassia Auriculata. *Colloids Surf B Biointerfaces* **2011**, *87*, 159–163, doi:10.1016/j.colsurfb.2011.05.016.
8. Flexa-Ribeiro, B.; Garcia, M.D.N.; Silva, A.C. de J.; Carvalho, J.C.T.; Rocha, L.; Faustino, S.M.M.; Fernandes, C.P.; da Silva, H.F.; Machado, F.P.; Hage-Melim, L.I. da S.; et al. Essential Oil from Curcuma Longa Leaves: Using Nanotechnology to Make a Promising Eco-Friendly Bio-Based Pesticide from Medicinal Plant Waste. *Molecules* **2025**, *30*, 1023, doi:10.3390/molecules30051023.

 doi:10.20944/preprints202508.0473.v1

9. Savković, Ž.; Džamić, A.; Veselinović, J.; Grbić, M.L.; Stupar, M. Exploring the Potential of Essential Oils against Airborne Fungi from Cultural Heritage Conservation Premises. *Science of Nature* **2025**, *112*, 32, doi:10.1007/s00114-025-01983-3.
10. Bautista-Hernández, I.; Gómez-García, R.; Martínez-Ávila, G.C.G.; Medina-Herrera, N.; González-Hernández, M.D. Unlocking Essential Oils' Potential as Sustainable Food Additives: Current State and Future Perspectives for Industrial Applications. *Sustainability (Switzerland)* **2025**, *17*, 2053, doi:10.3390/su17052053.
11. Omidian, H.; Cubeddu, L.X.; Gill, E.J. Harnessing Nanotechnology to Enhance Essential Oil Applications. *Molecules* **2025**, *30*, 520, doi:10.3390/molecules30030520.
12. Naeem, M.; Sana; Aftab, T.; Khan, M.M.A. Conclusions and Future Prospects of Plant-Based Essential Oils. In *Essential Oil-Bearing Plants: Agro-techniques, Phytochemicals, and Healthcare Applications*; Elsevier, 2025; pp. 381–384 ISBN 9780443248603.
13. Silva, E.F. da; Santos, F.A.L. dos; Pires, H.M.; Bastos, L.M.; Ribeiro, L.N. de M. Lipid Nanoparticles Carrying Essential Oils for Multiple Applications as Antimicrobials. *Pharmaceutics* **2025**, *17*, 178, doi:10.3390/pharmaceutics17020178.
14. Olaleru, S.A.; Molokwu, M.I.; Mathew, S.; Ejidike, I.P.; Oyebamiji, O.O. Enhanced Photocatalytic Degradation of Methylene Blue Dye Using TiO 2 Nanoparticles Obtained via Chemical and Green Synthesis: A Comparative Analysis. *Pure and Applied Chemistry* **2025**, *97*, 541–553, doi:10.1515/pac-2024-0326.
15. Ivanova, S.; Gvozdeva, Y.; Staynova, R.; Grekova-Kafalova, D.; Nalbantova, V.; Benbassat, N.; Koleva, N.; Ivanov, K. Essential Oils – a Review of the Natural Evolution of Applications and Some Future Perspectives. *Pharmacia* **2025**, *72*, 1–12, doi:10.3897/pharmacia.72.e140059.
16. Mishra, A.K.; Verma, S. Importance of Green Chemistry and Nano Techniques in Chemical Synthesis. In *Contemporary Trends in Chemical, Pharmaceutical and Life Sciences Volume V*; Bhumi Publishing: Pune, India, 2025; Vol. V, pp. 72–83 ISBN 978-93-48620-08-8.
17. Patadiya, A.; Mehta, D.; Karuppiah, N. Bridging Nature and Nanotechnology: A Review on the Potential of Herbal Nanoparticles in Medicine. *E3S Web of Conferences* **2025**, *619*, 05005, doi:10.1051/e3sconf/202561905005.
18. Sun, G.; Wang, L.; Dong, Z.; Zhang, Y.; Yang, Y.; Hu, M.; Fang, H. The Current Status, Hotspots, and Development Trends of Nanoemulsions: A Comprehensive Bibliometric Review. *Int J Nanomedicine* **2025**, *20*, 2937–2968, doi:10.2147/IJN.S502490.
19. Kirubakaran, D.; Wahid, J.B.A.; Karmegam, N.; Jeevika, R.; Sellapillai, L.; Rajkumar, M.; SenthilKumar, K.J. A Comprehensive Review on the Green Synthesis of Nanoparticles: Advancements in Biomedical and Environmental Applications. *Biomedical Materials and Devices* **2025**, doi:10.1007/s44174-025-00295-4.
20. Kirubakaran, D.; Bupesh, G.; Wahid, J.B.A.; Murugeswaran, R.; Ramalingam, J.; Arokiyaraj, S.; Sivasakthi, V.; Panigrahi, J. Green Synthesis of Zinc Oxide Nanoparticles Using Acmella Caulirhiza Leaf Extract: Characterization and Assessment of Antibacterial, Antioxidant, Anti-Inflammatory and Hemolytic Properties. *Biomedical Materials and Devices* **2025**, doi:10.1007/s44174-025-00283-8.
21. Sati, A.; Ranade, T.N.; Mali, S.N.; Ahmad Yasin, H.K.; Pratap, A. Silver Nanoparticles (AgNPs): Comprehensive Insights into Bio/Synthesis, Key Influencing Factors, Multifaceted Applications, and Toxicity—A 2024 Update. *ACS Omega* **2025**, *10*, 7549–7582, doi:10.1021/acsomega.4c11045.
22. Nagime, P. V; Shaikh, N.M.; Singh, S.; Chandak, V.S.; Chidrawar, V.R.; Nweye, E.P. Metallic Nanostructures: An Updated Review on Synthesis, Stability, Safety, and Applications with Tremendous Multifunctional Opportunities. *Pharm Nanotechnol* 2025, *13*, doi:10.2174/0122117385358312250108180301.
23. Soomro, R.; Abdelmonem, M.; Meli, A.D.; Panhwar, M.; Che Abdullah, C.A. A Novel Plant-Based Approach for Synthesis of Iron Oxide Nanoparticles and Cancer Therapy. *Discover Chemistry* **2025**, *2*, 25, doi:10.1007/s44371-025-00091-5.
24. Perveen, F.; Farmn Ullah; Assad Rehman; Haidar Zaman; Waseem Abbas; Muhammad Khan; Muhammad Bilal; Abbas Khan A Review on Nanotechnology-Driven Green Synthesis of Silver Nanoparticles Using Nigella Sativa. *Insights-Journal of Health and Rehabilitation* **2025**, *3*, 121–128, doi:10.71000/7k52p930.

 doi:10.20944/preprints202508.0473.v1

25. Shah, S.T.; Sari, I.P.; Yanto, D.H.Y.; Chowdhury, Z.Z.; Bashir, M.N.; Badruddin, I.A.; Hussien, M.; Lee, J.S. Nature's Nanofactories: Biogenic Synthesis of Metal Nanoparticles for Sustainable Technologies. *Green Chem Lett Rev* **2025**, *18*, doi:10.1080/17518253.2024.2448171.
26. Narduzzi, M.; Pelosi, C.; Vinciguerra, V.; Antonelli, C.; Vettraino, A.M. Natural Protection for Historic Mural Paintings: Thymus Serpyllum Essential Oil vs. Paracoccus IBR3 2025.
27. Abady, M.M.; Mohammed, D.M.; Soliman, T.N.; Shalaby, R.A.; Sakr, F.A. Sustainable Synthesis of Nanomaterials Using Different Renewable Sources. *Bull Natl Res Cent* **2025**, *49*, 24, doi:10.1186/s42269-025-01316-4.
28. Min, W. A Scientometric Review of Cultural Heritage Management and Sustainable Development through Evolutionary Perspectives. *npj Heritage Science* **2025**, *13*, 215, doi:10.1038/s40494-025-01708-9.
29. Srujana, T.L.; Rao, K.J.; Korumilli, T. Natural Biogenic Templates for Nanomaterial Synthesis: Advances, Applications, and Environmental Perspectives. *ACS Biomater Sci Eng* **2025**, *11*, 1291–1316, doi:10.1021/acsbiomaterials.4c02075.
30. Sachdeva, B.; Nisha, N.; Baby, N.; Aggarwal, K.; Singh, A.; Kumari, K.; Chandra, R.; Singh, S. Advancements in Silver-Based Nanocatalysts for Organic Transformations and Other Applications: A Comprehensive Review (2019-2024). *RSC Adv* **2025**, *15*, 17591–17634, doi:10.1039/d5ra00336a.
31. Kouadri, I.; Seghir, B. Ben; Cherif, N.F.; Rebiai, A. Nanomaterials Synthesis and Medicinal Plant Extracts. In *Interdisciplinary Biotechnological Advances*; 2025; Vol. 103, pp. 103–131.
32. Hamad, I.; Aleidi, S.M.; Alshaer, W.; Twal, S.; Al Olabi, M.; Bustanji, Y. Advancements and Global Perspectives in the Green Synthesis of Silver Nanoparticles: A Two-Decade Analysis. *Pharmacia* **2025**, *72*, 1–13, doi:10.3897/PHARMACIA.72.E142156.
33. Mangundu, P.; Makaudi, R.; Paumo, H.K.; Ramalapa, B.; Tshweu, L.; Raleie, N.; Katata-Seru, L. Plant-Derived Natural Products and Their Nano Transformation: A Sustainable Option Towards Desert Locust Infestations. *ChemistryOpen* **2025**, *14*, doi:10.1002/open.202400271.
34. Sarmah, K.; Anbalagan, T.; Marimuthu, M.; Mariappan, P.; Angappan, S.; Vaithiyanathan, S. Innovative Formulation Strategies for Botanical- and Essential Oil-Based Insecticides. *J Pest Sci (2004)* **2025**, *98*, 1–30, doi:10.1007/s10340-024-01846-2.
35. Yu, L.; Peng, J.; Han, Q.; Huang, W.; Jiang, Y.; Ruan, Y.; Liu, X.; Milcovich, G.; Weng, X. Encapsulation of Thyme Essential Oil in Dendritic Mesoporous Silica Nanoparticles: Enhanced Antimycotic Properties and ROS-Mediated Inhibition Mechanism. *Int J Pharm* **2025**, *669*, 125057, doi:10.1016/j.ijpharm.2024.125057.
36. Siam, A.M.J.; Abu-Zurayk, R.; Siam, N.; Abdelkheir, R.M.; Shibli, R. Forest Tree and Woody Plant-Based Biosynthesis of Nanoparticles and Their Applications. *Nanomaterials* **2025**, *15*, 845, doi:10.3390/nano15110845.
37. Xia, L.; Zhou, C.; Liu, X.; Yu, Y.; Xie, Q.; Lin, H.; Xiong, X.; Zhang, S.; Liang, W.; Shao, H. Transforming Bone Cancer Treatment: A Comprehensive Review of Green-Synthesized Metal Nanoparticles. *Cancer Cell International* **2025**, *25*, 193, doi:10.1186/s12935-025-03827-6.
38. Yao, Y.; Xu, Z.; Ding, H.; Yang, S.; Chen, B.; Zhou, M.; Zhu, Y.; Yang, A.; Yan, X.; Liang, C.; et al. Carrier-Free Nanoparticles—New Strategy of Improving Druggability of Natural Products. *Journal of Nanobiotechnology* **2025**, *23*, 108, doi:10.1186/s12951-025-03146-y.
39. Saghabashi, A.; Sadeghi, A.; Ghodratie, M.; hatami, H.; Alavi Rostami, S.F.; Yazdehi, M.; Mahmoudi, E.; Najafi, S.; Mottaghiyan, Z. Antimicrobial Potential of Satureja Species: A Review of Bioactive Compounds and Molecular Mechanisms. *Plant Biotechnology Persa* **2025**, *7*, 0–0, doi:10.61186/pbp.7.3.1.
40. Capdevila, S.; Grau, D.; Cristóbal, R.; Moré, E.; De las Heras, X. Chemical Composition of Wild Populations of Thymus Vulgaris and Satureja Montana in Central Catalonia, Spain. *JSFA reports* **2025**, *5*, 234–246, doi:10.1002/jsf2.70005.
41. Tancheva, L.; Dragomanova, S.; Abarova, S.; Grigorova, V.B.; Gavazova, V.; Stanciu, D.; Tzonev, S.; Kalfin, R. The Potential of Polyphenols Derived from Satureja Montana (Lamiaceae) in Prevention and Treatment of Various Mental Disorders, Including Dementia 2025.
42. Štrbac, F.; Krnjajić, S.; Ratajac, R.; Rinaldi, L.; Musella, V.; Castagna, F.; Stojanović, D.; Simin, N.; Orčić, D.; Bosco, A. Anthelmintic Activity of Winter Savory (Satureja Montana L.) Essential Oil against Gastrointestinal Nematodes of Sheep. *BMC Vet Res* **2025**, *21*, 405, doi:10.1186/s12917-025-04771-3.

 doi:10.20944/preprints202508.0473.v1

43. Zahraoui, E.M. Essential Oils: Antifungal Activity and Study Methods. *Moroccan Journal of Agricultural Sciences* **2025**, *6*, 99–108, doi:https://doi.org/10.5281/zenodo.15472437.
44. Shanaida, M.; Korablova, O.; Bakalets, D.; Potikha, N.; Rakhmetov, D. Chemotaxonomic Characteristics of Satureja Coerulea (Lamiaceae Family) Based on Analysis of Its Bioactive Compounds. *Biomedical and Pharmacology Journal* **2025**, *18*, 559–568, doi:10.13005/bpj/3108.
45. Demyashkin, G.; Parshenkov, M.; Tokov, A.; Sataieva, T.; Shevkoplyas, L.; Said, B.; Shamil, G. Therapeutic Efficacy of Plant-Based Hydrogels in Burn Wound Healing: Focus on Satureja Montana L. and Origanum Vulgare L. *Scr Med (Brno)* **2025**, *56*, 27–35, doi:10.5937/scriptamed56-56050.
46. Rai, M.K.; Kon, K.V. *Fighting Multidrug Resistance with Herbal Extracts, Essential Oils and Their Components*; Elsevier: Cambridge, MA, USA, 2013; ISBN 9780123985392.
47. Sahu, N.; Upadhyay, P. Phytochemical-Based Drugs for Salmonella Biofilm Disruption. In *Salmonella Biofilms: Formation, Resistance, and Therapeutics*; Publishing, B., Ed.; Royal Society of Chemistry: Maharashtra, India, 2025; pp. 123–143 ISBN 9781837677047.
48. Rinaldi, F.; Maurizi, L.; Conte, A.L.; Marazzato, M.; Maccelli, A.; Crestoni, M.E.; Hanieh, P.N.; Forte, J.; Conte, M.P.; Zagaglia, C.; et al. Nanoemulsions of Satureja Montana Essential Oil: Antimicrobial and Antibiofilm Activity against Avian Escherichia Coli Strains. *Pharmaceutics* **2021**, *13*, 134, doi:10.3390/pharmaceutics13020134.
49. Oliveira-Pinto, P.R.; Mariz-Ponte, N.; Sousa, R.M.O.F.; Torres, A.; Tavares, F.; Ribeiro, A.; Cavaco-Paulo, A.; Fernandes-Ferreira, M.; Santos, C. Satureja Montana Essential Oil, Zein Nanoparticles and Their Combination as a Biocontrol Strategy to Reduce Bacterial Spot Disease on Tomato Plants. *Horticulturae* **2021**, *7*, 584, doi:10.3390/horticulturae7120584.
50. Oliveira-Pinto, P.R.; Mariz-Ponte, N.; Gil, R.L.; Cunha, E.; Amorim, C.G.; Montenegro, M.C.B.S.M.; Fernandes-Ferreira, M.; Sousa, R.M.O.F.; Santos, C. Montmorillonite Nanoclay and Formulation with Satureja Montana Essential Oil as a Tool to Alleviate Xanthomonas Euvesicatoria Load on Solanum Lycopersicum. *Applied Nano* **2022**, *3*, 126–142, doi:10.3390/applnano3030009.
51. Sangeetha, A.; Ambli, A.; Nagabhushana, B.M. Green and Chemical Synthesis of TiO2 Nanoparticles: An In-Depth Comparative Analysis and Photoluminescence Study. *Nano-Structures & Nano-Objects* **2024**, *40*, 101408, doi:10.1016/j.nanoso.2024.101408.
52. Pham, D.Q.; Chu, T. Van; Phan, H.T.; Nguyen, S.V.; Le, T.T.; Tran, D.Q.; Nguyen, H.K.; Vo, A.T.K.; Tran, L.D.; Tran, K.N.; et al. Antifungal Nanoformulation of Botanical Anthraquinone and TiO2 against Melon Phytopathogenic Fungi: Preparation, in Vitro Bioassays and Field Test. *Not Bot Horti Agrobot Cluj Napoca* **2025**, *53*, 14108, doi:10.15835/nbha53114108.
53. Wang, Y.; Zhang, Y.; Ma, Y.; Liu, J.; Zhang, R.; Zhao, J. Preparation and Application of Chitosan/Nano-TiO_2/Daisy Essential Oil Composite Films in the Preservation of Actinidia Arguta. *Food Chem X* **2025**, *26*, 102303, doi:10.1016/j.fochx.2025.102303.
54. Macedo, C.; Costa, P.C.; Rodrigues, F. Bioactive Compounds from Actinidia Arguta Fruit as a New Strategy to Fight Glioblastoma. *Food Research International* **2024**, *175*, 113770, doi:10.1016/j.foodres.2023.113770.
55. Shakeel, N.; Piwoński, I.; Iqbal, P.; Kisielewska, A. Green Synthesis of Titanium Dioxide Nanoparticles: Physicochemical Characterization and Applications: A Review. *Int J Mol Sci* **2025**, *26*, 5454, doi:10.3390/ijms26125454.
56. Wollenweber, E.; Dörr, M.; Rustaiyan, A.; Roitman, J.N.; Graven, E.H. Notes: Exudate Flavonoids of Some Salvia and a Trichostema Species. *Zeitschrift für Naturforschung C* **1992**, *47*, 782–784, doi:10.1515/znc-1992-9-1025.
57. Ghadiri Soltan Meydan, T.; Samareh Moosavi, S.; Sabouri, Z.; Darroudi, M. Green Synthesis of CaCO3 Nanoparticles for Photocatalysis and Cytotoxicity. *Bioprocess Biosyst Eng* **2023**, *46*, 727–734, doi:10.1007/s00449-023-02859-4.
58. Nelwamondo, A.M.; Kaningini, A.G.; Ngmenzuma, T.Y.; Maseko, S.T.; Maaza, M.; Mohale, K.C. Biosynthesis of Magnesium Oxide and Calcium Carbonate Nanoparticles Using Moringa Oleifera Extract and Their Effectiveness on the Growth, Yield and Photosynthetic Performance of Groundnut (Arachis Hypogaea L.) Genotypes. *Heliyon* **2023**, *9*, e19419, doi:10.1016/j.heliyon.2023.e19419.

 doi:10.20944/preprints202508.0473.v1

59. Frassine, D.; Braglia, R.; Scuderi, F.; Redi, E.L.; Valentini, F.; Relucenti, M.; Colasanti, I.A.; Macchia, A.; Allegrini, I.; Gismondi, A.; et al. Enhancing Lettuce (Lactuca Sativa) Productivity: Foliar Sprayed Fe-Alg-CaCO3 MPs as Fertilizers for Aquaponics Cultivation. *Plants* **2024**, *13*, 3416, doi:10.3390/plants13233416.
60. Valentini, F.; Pallecchi, P.; Relucenti, M.; Donfrancesco, O.; Sottili, G.; Pettiti, I.; Mussi, V. Characterization of Calcium Carbonate Nanoparticles with Architectural Application for the Consolidation of Pietraforte. *Anal Lett* **2022**, *55*, 93–108, doi:10.1080/00032719.2021.1918138.
61. Frassine, D.; Braglia, R.; Scuderi, F.; Redi, E.L.; Valentini, F.; Relucenti, M.; Colasanti, I.A.; Zaratti, C.; Macchia, A.; Allegrini, I.; et al. Smart Foliar Fertilizer Based on Zn-Alg-$CaCO_3$ Microparticles Improves Aquaponic Tomato Cultivation. *Sci Rep* **2025**, *15*, 18092, doi:10.1038/s41598-025-03136-y.
62. Valentini, F.; Bertini, F.; Carbone, M.; Antiochia, R.; Favero, G.; Boaretto, A.; Gazzoli, D. Calcite Nanoparticles as Possible Nano-Fillers for Reinforcing the Plaster of Palazzetto Alessandro Lancia in Rome. *European Journal of Science and Theology* **2016**, *12*, 245–259.
63. Bicchieri, M.; Valentini, F.; Calcaterra, A.; Talamo, M. Newly Developed Nano-Calcium Carbonate and Nano-Calcium Propanoate for the Deacidification of Library and Archival Materials. *J Anal Methods Chem* **2017**, *2017*, 2372789, doi:10.1155/2017/2372789.
64. Li, L.; Yao, Y.; Fu, N. Free Carboxylic Acids: The Trend of Radical Decarboxylative Functionalization. *European J Org Chem* **2023**, *26*, e202300166, doi:10.1002/EJOC.202300166;WGROUP:STRING:PUBLICATION.
65. Ju, S.; Singh, M.K.; Han, S.; Ranbhise, J.; Ha, J.; Choe, W.; Yoon, K.S.; Yeo, S.G.; Kim, S.S.; Kang, I. Oxidative Stress and Cancer Therapy: Controlling Cancer Cells Using Reactive Oxygen Species. *Int J Mol Sci* 2024, *25*, doi:10.3390/IJMS252212387,.
66. Kheamrutai Thamaphat; Limsuwan, P.; Boonlaer Ngotawornchai Phase Characterization of TiO_2 Powder by XRD and TEM. *Kasetsart Journal (Natural Science)* **2008**, *42*, 357–361.
67. You, Y.F.; Xu, C.H.; Xu, S.S.; Cao, S.; Wang, J.P.; Huang, Y.B.; Shi, S.Q. Structural Characterization and Optical Property of TiO2 Powders Prepared by the Sol-Gel Method. *Ceram Int* **2014**, *40*, 8659–8666, doi:10.1016/j.ceramint.2014.01.083.
68. El-Sheikh, S.M.; Khedr, T.M.; Zhang, G.; Vogiazi, V.; Ismail, A.A.; O'Shea, K.; Dionysiou, D.D. Tailored Synthesis of Anatase–Brookite Heterojunction Photocatalysts for Degradation of Cylindrospermopsin under UV–Vis Light. *Chemical Engineering Journal* **2017**, *310*, 428–436, doi:10.1016/j.cej.2016.05.007.
69. Bellardita, M.; Di Paola, A.; Megna, B.; Palmisano, L. Absolute Crystallinity and Photocatalytic Activity of Brookite TiO2 Samples. *Appl Catal B* **2017**, *201*, 150–158, doi:10.1016/j.apcatb.2016.08.012.
70. Rezaee, M.; Mousavi Khoie, S.M.; Liu, K.H. The Role of Brookite in Mechanical Activation of Anatase-to-Rutile Transformation of Nanocrystalline TiO2: An XRD and Raman Spectroscopy Investigation. *CrystEngComm* **2011**, *13*, 5055–5061, doi:10.1039/c1ce05185g.
71. Yan, J.; Wu, G.; Guan, N.; Li, L.; Li, Z.; Cao, X. Understanding the Effect of Surface/Bulk Defects on the Photocatalytic Activity of TiO2: Anatase versus Rutile. *Physical Chemistry Chemical Physics* **2013**, *15*, 10978–10988, doi:10.1039/c3cp50927c.
72. Kandiel, T.A.; Robben, L.; Alkaima, A.; Bahnemann, D. Brookite versus Anatase TiO2 Photocatalysts: Phase Transformations and Photocatalytic Activities. *Photochemical & Photobiological Sciences* **2013**, *12*, 602–609, doi:10.1039/c2pp25217a.
73. Hu, W.; Li, L.; Li, G.; Tang, C.; Sun, L. High-Quality Brookite TiO2 Flowers: Synthesis, Characterization, and Dielectric Performance. *Cryst Growth Des* **2009**, *9*, 3676–3682, doi:10.1021/cg9004032.
74. Anjos, O.; Santos, A.J.A.; Paixão, V.; Estevinho, L.M. Physicochemical Characterization of Lavandula Spp. Honey with FT-Raman Spectroscopy. *Talanta* **2018**, *178*, 43–48, doi:10.1016/j.talanta.2017.08.099.
75. Espina, A.; Sanchez-Cortes, S.; Jurašeková, Z. Vibrational Study (Raman, SERS, and IR) of Plant Gallnut Polyphenols Related to the Fabrication of Iron Gall Inks. *Molecules* **2022**, *27*, 279, doi:10.3390/molecules27010279.
76. Minteguiaga, M.; Dellacassa, E.; Iramain, M.A.; Catalán, C.A.N.; Brandán, S.A. FT-IR, FT-Raman, UV–Vis, NMR and Structural Studies of Carquejyl Acetate, a Distinctive Component of the Essential Oil from Baccharis Trimera (Less.) DC. (Asteraceae). *J Mol Struct* **2019**, *1177*, 499–510, doi:10.1016/j.molstruc.2018.10.010.

77. Vargas Jentzsch, P.; Sandoval Pauker, C.; Zárate Pozo, P.; Sinche Serra, M.; Jácome Camacho, G.; Rueda-Ayala, V.; Garrido, P.; Ramos Guerrero, L.; Ciobotă, V. Raman Spectroscopy in the Detection of Adulterated Essential Oils: The Case of Nonvolatile Adulterants. *Journal of Raman Spectroscopy* **2021**, *52*, 1055–1063, doi:10.1002/jrs.6089.
78. Calheiros, R.; Machado, N.F.L.; Fiuza, S.M.; Gaspar, A.; Garrido, J.; Milhazes, N.; Borges, F.; Marques, M.P.M. Antioxidant Phenolic Esters with Potential Anticancer Activity: A Raman Spectroscopy Study. *Journal of Raman Spectroscopy* **2008**, *39*, 95–107, doi:10.1002/jrs.1822.
79. Schulz, H.; Özkan, G.; Baranska, M.; Krüger, H.; Özcan, M. Characterisation of Essential Oil Plants from Turkey by IR and Raman Spectroscopy. *Vib Spectrosc* **2005**, *39*, 249–256, doi:10.1016/j.vibspec.2005.04.009.
80. Lafhal, S.; Vanloot, P.; Bombarda, I.; Valls, R.; Kister, J.; Dupuy, N. Raman Spectroscopy for Identification and Quantification Analysis of Essential Oil Varieties: A Multivariate Approach Applied to Lavender and Lavandin Essential Oils. *Journal of Raman Spectroscopy* **2015**, *46*, 577–585, doi:10.1002/jrs.4697.
81. Rodríguez-Solana, R.; Daferera, D.J.; Mitsi, C.; Trigas, P.; Polissiou, M.; Tarantilis, P.A. Comparative Chemotype Determination of Lamiaceae Plants by Means of GC-MS, FT-IR, and Dispersive-Raman Spectroscopic Techniques and GC-FID Quantification. *Ind Crops Prod* **2014**, *62*, 22–33, doi:10.1016/j.indcrop.2014.08.003.
82. Ram Kumar, A.; Selvaraj, S.; Azam, M.; Sheeja Mol, G.; Kanagathara, N.; Alam, M.; Jayaprakash, P. Spectroscopic, Biological, and Topological Insights on Lemonol as a Potential Anticancer Agent. *ACS Omega* **2023**, *8*, 31548–31566, doi:10.1021/acsomega.3c04922.
83. Ertani, A.; Pizzeghello, D.; Francioso, O.; Tinti, A.; Nardi, S. Biological Activity of Vegetal Extracts Containing Phenols on Plant Metabolism. *Molecules* **2016**, *21*, 205, doi:10.3390/molecules21020205.
84. Yang, M.; Han, L.; Xu, Y.; Ke, H.; Zhou, N.; Dong, H.; Liu, S.; Qiao, G. Near Infrared Spectroscopic Study of Trioctahedral Chlorites and Its Remote Sensing Application. *Open Geosciences* **2019**, *11*, 815–828, doi:10.1515/geo-2019-0063.
85. Blessymol, B.; Yasotha, P.; Kalaiselvi, V.; Gopi, S. An Antioxidant Study of Titanium Dioxide (TiO2) Nanoparticles against Mace of Nutmeg in Myristica Fragrans Houtt, Rhizomes of Curcuma Longa Linn and Kaempferia Galanga Extracts. *Results Chem* **2024**, *7*, 101291, doi:10.1016/j.rechem.2023.101291.
86. Pushpamalini, T.; Keerthana, M.; Sangavi, R.; Nagaraj, A.; Kamaraj, P. Comparative Analysis of Green Synthesis of TiO2 Nanoparticles Using Four Different Leaf Extract. *Mater Today Proc* **2021**, *40*, S180–S184, doi:10.1016/j.matpr.2020.08.438.
87. Ahmadi, O.; Jafarizadeh-Malmiri, H. Intensification Process in Thyme Essential Oil Nanoemulsion Preparation Based on Subcritical Water as Green Solvent and Six Different Emulsifiers. *Green Processing and Synthesis* **2021**, *10*, 430–439, doi:10.1515/gps-2021-0040.
88. Agatonovic-Kustrin, S.; Ristivojevic, P.; Gegechkori, V.; Litvinova, T.M.; Morton, D.W. Essential Oil Quality and Purity Evaluation via Ft-Ir Spectroscopy and Pattern Recognition Techniques. *Applied Sciences (Switzerland)* **2020**, *10*, 1–12, doi:10.3390/app10207294.
89. Abdallah, R.A.; El-Borady, O.M.; El-Sayed, A.F.; Fawzy, M. A Comparative Study of Chemo- and Phytosynthesized Silver Nanoparticles Using Ceratophyllum Demersum Extract: Characterization and Biological Activities. *Biomass Convers Biorefin* **2025**, doi:10.1007/s13399-025-06718-y.
90. Falcioni, R.; Moriwaki, T.; Gibin, M.S.; Vollmann, A.; Pattaro, M.C.; Giacomelli, M.E.; Sato, F.; Nanni, M.R.; Antunes, W.C. Classification and Prediction by Pigment Content in Lettuce (Lactuca Sativa L.) Varieties Using Machine Learning and ATR-FTIR Spectroscopy. *Plants* **2022**, *11*, 3413, doi:10.3390/plants11243413.
91. Silverstein, R.M.; Webster, F.X.; Kiemle, D. *Spectrometric Identification of Organic Compounds*; 7th Editio.; Wiley: Hoboken, New Jersey, United States, 2005; ISBN 1118311655.
92. Juhasz-Bortuzzo, J.A.; Myszka, B.; Silva, R.; Boccaccini, A.R. Sonosynthesis of Vaterite-Type Calcium Carbonate. *Cryst Growth Des* **2017**, *17*, 2351–2356, doi:10.1021/acs.cgd.6b01493.
93. Zhou, G.T.; Yu, J.C.; Wang, X.C.; Zhang, L.Z. Sonochemical Synthesis of Aragonite-Type Calcium Carbonate with Different Morphologies. *New Journal of Chemistry* **2004**, *28*, 1027–1031, doi:10.1039/b315198k.

 doi:10.20944/preprints202508.0473.v1

94. Ramasamy, V.; Anand, P.; Suresh, G. Synthesis and Characterization of Polymer-Mediated CaCO3 Nanoparticles Using Limestone: A Novel Approach. *Advanced Powder Technology* **2018**, *29*, 818–834, doi:10.1016/j.apt.2017.12.023.
95. Swain, S.K.; Pradhan, G.C.; Dash, S.; Mohanty, F.; Behera, L. Preparation and Characterization of Bionanocomposites Based on Soluble Starch/Nano CaCO3. *Polym Compos* **2018**, *39*, E82–E89, doi:10.1002/pc.24326.
96. Kim, Y.; Caumon, M.C.; Barres, O.; Sall, A.; Cauzid, J. Identification and Composition of Carbonate Minerals of the Calcite Structure by Raman and Infrared Spectroscopies Using Portable Devices. *Spectrochim Acta A Mol Biomol Spectrosc* **2021**, *261*, 119980, doi:10.1016/j.saa.2021.119980.
97. Alves, J.F.; Edwards, H.G.M.; Korsakov, A.; de Oliveira, L.F.C. Revisiting the Raman Spectra of Carbonate Minerals. *Minerals* **2023**, *13*, 1358, doi:10.3390/min13111358.
98. Legodi, M.A.; De Waal, D.; Potgieter, J.H. Quantitative Determination of CaCO3 in Cement Blends by FT-IR. *Appl Spectrosc* **2001**, *55*, 361–365, doi:10.1366/0003702011951786.
99. Vagenas, N. V.; Gatsouli, A.; Kontoyannis, C.G. Quantitative Analysis of Synthetic Calcium Carbonate Polymorphs Using FT-IR Spectroscopy. *Talanta* **2003**, *59*, 831–836, doi:10.1016/S0039-9140(02)00638-0.
100. Gismondi, A.; Di Marco, G.; Redi, E.L.; Ferrucci, L.; Cantonetti, M.; Canini, A. The Antimicrobial Activity of Lavandula Angustifolia Mill. Essential Oil against Staphylococcus Species in a Hospital Environment. *J Herb Med* **2021**, *26*, doi:10.1016/j.hermed.2021.100426.
101. Sundaram, T.; Rajendran, S.; Natarajan, S.; Vinayagam, S.; Rajamohan, R.; Lackner, M. Environmental Fate and Transformation of TiO_2 Nanoparticles: A Comprehensive Assessment. *Alexandria Engineering Journal* **2025**, *115*, 264–276.
102. Khalaf Kenawe, L.; Abbas, R.S.; Kadhim, A.S. Comparative Study of Alcohol Clove Extract, TiO2 Nanoparticles, and Clove Extract-TiO2 Complex in Controlling Bacterial Growth in Burn Infections. *Microbes and Infectious Diseases* **2025**, *6*, 680–688, doi:10.21608/mid.2024.309810.2131.
103. Fletes-Vargas, G.; Rodríguez-Rodríguez, R.; Pinto, N.V.; Kato, K.C.; Carneiro, G.; Rodrigues, A.P.; Rodrigues-Martins, H.; Espinosa-Andrews, H. TiO2 Nanoparticles Loaded with Polygonum Cuspidatum Extract for Wound Healing Applications: Exploring Their Hemolytic, Antioxidant, Cytotoxic, and Antimicrobial Properties. *Nanomaterials* **2025**, *15*, 926, doi:10.3390/nano15120926.
104. Al-darwesh, M.Y.; Babakr, K.A.; Qader, I.N.; Mohammed, M.A. Antimicrobial, Anti-Inflammatory, and Anticancer Potential of Green Synthesis TiO2 Nanoparticles Using Sophora Flavescens Root Extract. *Chemical Papers* **2025**, *79*, 1207–1221, doi:10.1007/s11696-024-03853-0.
105. Raj, L.F.A.A.; Annushrie, A.; Namasivayam, S.K.R. Anti Bacterial Efficacy of Photo Catalytic Active Titanium Di Oxide (TiO2) Nanoparticles Synthesized via Green Science Principles against Food Spoilage Pathogenic Bacteria. *Microbe (Netherlands)* **2025**, *7*, doi:10.1016/j.microb.2025.100331.
106. Shah, R.R.; Kaewgun, S.; Lee, B.I.; Tzeng, T.R.J. The Antibacterial Effects of Biphasic Brookite-Anatase Titanium Dioxide Nanoparticles on Multiple-Drug-Resistant Staphylococcus Aureus. In Proceedings of the Journal of Biomedical Nanotechnology; September 2008; Vol. 4, pp. 339–348.
107. Delgado, L.P.; Figueroa-Torres, M.Z.; Ceballos-Chuc, M.C.; García-Rodríguez, R.; Alvarado-Gil, J.J.; Oskam, G.; Rodriguez-Gattorno, G. "Tailoring the TiO2 Phases through Microwave-Assisted Hydrothermal Synthesis: Comparative Assessment of Bactericidal Activity." *Materials Science and Engineering C* **2020**, *117*, doi:10.1016/j.msec.2020.111290.
108. Zhang, C.; Dabbs, D.M.; Liu, L.M.; Aksay, I.A.; Car, R.; Selloni, A. Combined Effects of Functional Groups, Lattice Defects, and Edges in the Infrared Spectra of Graphene Oxide. *Journal of Physical Chemistry C* **2015**, *119*, 18167–18176, doi:10.1021/acs.jpcc.5b02727.
109. Nguyet Nga, D.T.; Le Nhat Trang, N.; Hoang, V.T.; Ngo, X.D.; Nhung, P.T.; Tri, D.Q.; Cuong, N.D.; Tuan, P.A.; Huy, T.Q.; Le, A.T. Elucidating the Roles of Oxygen Functional Groups and Defect Density of Electrochemically Exfoliated GO on the Kinetic Parameters towards Furazolidone Detection. *RSC Adv* **2022**, *12*, 27855–27867, doi:10.1039/D2RA04147B.
110. Mardente, S.; Aventaggiato, M.; Splendiani, E.; Mari, E.; Zicari, A.; Catanzaro, G.; Po, A.; Coppola, L.; Tafani, M. Extra-Cellular Vesicles Derived from Thyroid Cancer Cells Promote the Epithelial to Mesenchymal

 doi:10.20944/preprints202508.0473.v1

Transition (EMT) and the Transfer of Malignant Phenotypes through Immune Mediated Mechanisms. *Int J Mol Sci* **2023**, *24*, doi:10.3390/ijms24032754.

111. Chen, X.; Liao, D.; Zhou, Q.; Li, X.; Sun, J.; Tong, Z.; Lai, L.; Sun, L.; Zhou, G. Hollow Calcium Carbonate Microspheres Prepared from Waste Eggshells as PH-Responsive Controlled-Release Carvacrol for Efficient and Safe Antimicrobial Agents in Pork Preservation. *Food Control* **2025**, *176*, doi:10.1016/j.foodcont.2025.111347.
112. Koley, R.; Mandal, M.; Mondal, A.; Debnath, P.; Mondal, A.; Mondal, N.K. Synthesis of Calcium Carbonate Nanoparticles from Mollusc Shell Waste and Its Efficacy towards Plant Growth and Development. *Sustainable Chemistry One World* **2025**, *6*, doi:10.1016/j.scowo.2025.100056.
113. Motlhalamme, T.; Mohamed, H.; Kaningini, A.G.; More, G.K.; Thema, F.T.; Mohale, K.C.; Maaza, M. Bio-Synthesized Calcium Carbonate (CaCO3) Nanoparticles: Their Anti-Fungal Properties and Application as Nanofertilizer on Lycopersicon Esculentum Growth and Gas Exchange Measurements. *Plant Nano Biology* **2023**, *6*, 100050, doi:10.1016/j.plana.2023.100050.
114. Motlhalamme, T.; Kaningini, A.G.; Thema, F.T.; Mohale, K.C.; Maaza, M. Nanotechnology in Agriculture: Exploring the Influence of Calcium Carbonate Nanoparticles on Tomato Leaf and Fruit Metabolomic Profiles. *South African Journal of Botany* **2025**, *180*, 615–624, doi:10.1016/j.sajb.2025.03.028.
115. Wesolowska, A.; Grzeszczuk, M.; Jadczak, D. Influence of Harvest Term on the Content of Carvacrol, p-Cymene, Î³-Terpinene and Î²-Caryophyllene in the Essential Oil of Satureja Montana. *Not Bot Horti Agrobot Cluj Napoca* **2014**, *42*, 392–397, doi:10.15835/nbha4229645.
116. Serrano, C.; Matos, O.; Teixeira, B.; Ramos, C.; Neng, N.; Nogueira, J.; Nunes, M.L.; Marques, A. Antioxidant and Antimicrobial Activity of Satureja Montana L. Extracts. *J Sci Food Agric* **2011**, *91*, 1554–1560, doi:10.1002/jsfa.4347.
117. Aravind, M.; Amalanathan, M.; Mary, M. Synthesis of TiO2 Nanoparticles by Chemical and Green Synthesis Methods and Their Multifaceted Properties. *SN Appl Sci* **2021**, *3*, 1–10, doi:10.1007/S42452-021-04281-5.
118. Bahrom, H.; Goncharenko, A.A.; Fatkhutdinova, L.I.; Peltek, O.O.; Muslimov, A.R.; Koval, O.Y.; Eliseev, I.E.; Manchev, A.; Gorin, D.; Shishkin, I.I.; et al. Controllable Synthesis of Calcium Carbonate with Different Geometry: Comprehensive Analysis of Particle Formation, Cellular Uptake, and Biocompatibility. *ACS Sustain Chem Eng* **2019**, *7*, 19142–19156, doi:10.1021/acssuschemeng.9b05128.
119. Garg, R.; Kumari, M.; Kumar, M.; Dhiman, S.; Garg, R. Green Synthesis of Calcium Carbonate Nanoparticles Using Waste Fruit Peel Extract. *Mater Today Proc* **2021**, *46*, 6665–6668, doi:10.1016/j.matpr.2021.04.124.
120. Correr, S.; Makabe, S.; Heyn, R.; Relucenti, M.; Naguro, T.; Familiari, G. Microplicae-like Structures of the Fallopian Tube in Postmenopausal Women as Shown by Electron Microscopy. *Histol Histopathol* **2006**, *21*, 219–226, doi:10.14670/HH-21.219.
121. Relucenti, M.; Heyn, R.; Correr, S.; Familiari, G. Cumulus Oophorus Extracellular Matrix in the Human Oocyte: A Role for Adhesive Proteins. In Proceedings of the Italian Journal of Anatomy and Embryology; 2005; Vol. 110, pp. 219–224.
122. Relucenti, M.; Heyn, R.; Petruzziello, L.; Pugliese, G.; Taurino, M.; Familiari, G. Detecting Microcalcifications in Atherosclerotic Plaques by a Simple Trichromic Staining Method for Epoxy Embedded Carotid Endarterectomies. *European Journal of Histochemistry* **2010**, *54*, 143–147, doi:10.4081/ejh.2010.e33.
123. Di Giorgio, G.; Relucenti, M.; Iaculli, F.; Salucci, A.; Donfrancesco, O.; Polimeni, A.; Bossù, M. The Application of a Fluoride-and-Vitamin D Solution to Deciduous Teeth Promotes Formation of Persistent Mineral Crystals: A Morphological Ex-Vivo Study. *Materials* **2023**, *16*, doi:10.3390/ma16114049.
124. Bossù, M.; Matassa, R.; Relucenti, M.; Iaculli, F.; Salucci, A.; Di Giorgio, G.; Familiari, G.; Polimeni, A.; Di Carlo, S. Morpho-Chemical Observations of Human Deciduous Teeth Enamel in Response to Biomimetic Toothpastes Treatment. *Materials* **2020**, *13*, doi:10.3390/MA13081803.
125. Viani, I.; Colucci, M.E.; Pergreffi, M.; Rossi, D.; Veronesi, L.; Bizzarro, A.; Capobianco, E.; Affanni, P.; Zoni, R.; Saccani, E.; et al. Passive Air Sampling: The Use of the Index of Microbial Air Contamination. *Acta Biomedica* **2020**, *91*, 92–105, doi:10.23750/abm.v91i3-S.9434.

 doi:10.20944/preprints202508.0473.v1

126. Pasquarella, C.; Pitzurra, O.; Savino, A. The Index of Microbial Air Contamination. *Journal of Hospital Infection* **2000**, *46*, 241–256.